

Planar hydraulic fracture growth perpendicular to the isotropy plane in a transversely isotropic material

Fatima-Ezzahra Moukhtari^a, Brice Lecampion^{a,*}, Haseeb Zia^a

^a*Geo-Energy Laboratory- Gaznat chair on Geo-Energy, EPFL,
ENAC-IIC-GEL-EPFL, Station 18, Lausanne CH-1015, Switzerland*

Abstract

The configuration of a hydraulic fracture (HF) propagating perpendicular to the isotropy plane of a transversely isotropic (TI) material is encountered in most sedimentary basins. We account for both elastic and fracture toughness anisotropy, and investigate fracture growth driven by the injection of a Newtonian fluid at a constant rate from a point source. In addition to the usual dimensionless parameters governing HF growth in isotropy, four dimensionless elastic parameters enter the problem for a TI material: the ratio β of elastic plane-strain modulus in the two orthogonal directions of the material frame, two Thomsen parameters ϵ , δ and the stiffness ratio C_{13}/C_{11} . Moreover, the ratio κ of fracture toughness in the two orthogonal directions as well as the details of the toughness anisotropy also plays a role on the development of the fracture geometry. We quantify HF growth numerically without any a-priori assumptions on the fracture shape. In doing so, we derive the exact expression for the near-tip elastic modulus as a function of propagation direction and extend to TI an implicit level set algorithm coupling a finite discretization with the near-tip solution for a steadily moving HF. A solution for a toughness dominated elliptical HF in a TI material is derived and used to verify our numerical solver. Importantly, the fracture shape is strictly elliptical only for a very peculiar form of toughness anisotropy. The evolution of the HF from the viscosity dominated regime (early time) to the toughness dominated regime (late time) results in an increase of the fracture elongation. The elongation of the fracture in the viscosity dominated regime scales as $0.76\beta^{-1/3}$ and increases as the propagation transition to the toughness dominated regime. We confirm the expressions for the transition time-scales in the two orthogonal directions of the material frame obtained from scaling considerations. The exact form of the toughness anisotropy plays a crucial role on the final fracture elongation in the toughness regime, which scales as β^{-2} for the case of an isotropic toughness, β^{-1} for an isotropic fracture energy and as $(\kappa/\beta)^2$ for the peculiar case of an 'elliptical' fracture anisotropy. Our results also indicate that i) simplified approximations for the near-tip modulus previously derived are only valid for weak anisotropy ($\beta < 1.2$) and that ii) the other elastic parameters have a second order effect on HF growth (at most 10 percent).

Keywords: A. fracture, B. anisotropic material, B. rock, C. boundary integral equations, C. numerical algorithms

*Corresponding author: brice.lecampion@epfl.ch

1. Introduction

Transverse isotropy (TI) is an ubiquitous feature of sedimentary rocks. It is a direct result of the sedimentation process and occurs over a wide range of scales. In particular, shales and mudstones are the results of fine layers deposit of micro-meters to centimeters thickness whose constituents may also be intrinsically anisotropic (Bobko and Ulm, 2008; Sone and Zoback, 2013). Placing ourselves at the continuum level, we model these rocks as transversely isotropic and study in details the growth of a planar three-dimensional fluid-driven fracture perpendicular to the isotropy plane. Such a configuration notably corresponds to the case where the intrinsic rock layering is horizontal and the fracture grows vertically (see Fig. 1). This is notably the case in a large number of sedimentary basins which exhibit a normal or a strike-slip in-situ stress regime where the minimum principal stress direction is horizontal. Minimizing energy spent, the fracture thus grows in the vertical plane perpendicular to the material isotropy plane (Hubbert and Willis, 1957). In the presence of weak bedding planes (isotropy plane), the fracture may possibly deviates from the vertical direction resulting in T-shape like geometries, or exhibit several jogs/horizontal offset (Bunger and Lecampion, 2017). We do not account for this possibility here and strictly restrict our investigation to cases where the fracture grows in a single plane perpendicular to the material isotropy plane. This corresponds to the limit of either i) very strong isotropy / bedding planes or ii) very large in-situ compressive stress normal to the isotropy / bedding plane (i.e. $\sigma_v \gg \sigma_h$ in the configuration of Fig. 1). In that limit, how a fluid driven fracture originating from a point source develops as function of the material anisotropy and injection parameters (fluid viscosity, injection rate) remains only partly understood. One of the main questions relates to the elongation of the fracture in the horizontal direction when transverse elastic isotropy is accounted for (Zia et al., 2018). Laubie and Ulm (2014) have investigated the problem of a strictly elliptical fracture in the so-called toughness dominated regime where dissipation associated with viscous fluid flow in the fracture is negligible. Using a simplified approach based on Hoenig (1978) solution for an elliptical crack, they have notably obtained a relationship between the aspect ratio of the equilibrium fracture and the ratio of the plane-strain elastic modulus in the 1 and 3 directions. Bessmertnykh and Dontsov (2018) have further obtained an approximation for the fracture elongation (assuming an elliptical shape) for the case of a fracture driven by Herschel-Bulkley fluid in both the viscosity and toughness dominated regimes. Assuming the same ideal elliptical fracture geometry, scaling laws and approximated growth solutions were recently obtained (Dontsov, 2019).

In this contribution, we investigate the problem numerically in combination with a scaling analysis. We do not impose any a-priori constraint on the fracture shape and do not make any simplifications in our handling of elastic transverse isotropy. This will notably allow to quantify some of the approximations previously put forward (Laubie and Ulm, 2014; Bessmertnykh and Dontsov, 2018; Dontsov, 2019). We extend a fully-coupled implicit level set algorithm for hydraulic fracture growth (Peirce and Detournay, 2008) to account for material transverse isotropy both in terms of elasticity and possibly fracture energy. We restrict to the case of low permeability materials and neglect fluid leak-off in the surrounding rock for clarity. Following the classical hydraulic fracture mechanics model, we account for viscous fluid flow in the fracture coupled to mechanical deformation and a linear elastic fracture mechanics criteria for quasi-static growth. One of the peculiarity of hydraulic fractures lie in the competition between the energy dissipation associated

	C_{11}	C_{33}	C_{12}	C_{13}	C_{44}
Olkiluoto mica gneiss (Hakala et al., 2007)	89.7	65.9	22.2	23.5	24
Gas-saturated Shaly Coal (Wang, 2002)	22.1	10.9	8.36	1.2	3.7
Woodford53 shale (Laubie, 2013)	28	17.3	7.5	8.3	5.6
Opalinus Clay (Thöny, 2014)	57.6	28.8	54.6	38.7	0.9
Yeocheon schist (Cho et al., 2012)	91.4	27.6	33.7	20	13.7
Calcareous mudstone (Chertov, 2012)	90.4	35.1	51.6	39.8	6.5

Table 1: Examples of elastic stiffness coefficients (Voigt notation) of different transversely isotropic (TI) rocks - all values in GPa.

with viscous flow and the one associated with the creation of new fracture surfaces. This competition is well understood for an isotropic material and results in very different propagation regimes: either viscosity or toughness dominated (Detournay, 2004, 2016). Moreover, this competition between viscosity and toughness dissipation results in a multi-scale structure of the near-tip region (Garagash et al., 2011) which is extremely difficult to resolve accurately using naive discretization techniques (Lecampion et al., 2013, 2018). Such a near-tip solution for a steadily moving hydraulic fracture can be combined with a finite scale discretization of the fracture, yielding very efficient numerical schemes (Peirce, 2015, 2016).

In the following, we first briefly recall the ingredients of the planar hydraulic fracture (HF) model highlighting the differences brought by transverse isotropy (TI). We then obtain an exact expression for the near-tip elastic operator as a function of propagation direction in a TI material. More precisely, we obtain the near-tip plane-strain elastic modulus entering the so-called Irwin matrix relating co-planar energy release rate and stress intensity factors (Barnett and Asaro, 1972). This enables the extension of the near-tip fluid-driven asymptotic solution to transverse isotropy (TI), and its use in a fully coupled numerical scheme as a result. We also obtain an exact analytical solution for an elliptical hydraulic fracture propagating in the toughness dominated regime. This notably allows to benchmark our simulator for a peculiar case of toughness anisotropy (leading to an elliptical fracture shape). Combining a scaling analysis and numerical simulations, we quantify the growth of a hydraulic fracture in both toughness dominated and viscosity dominated growth in a TI elastic medium under different assumptions on the anisotropy of fracture toughness (isotropic toughness versus isotropic fracture energy vs elliptical toughness anisotropy). We finally explore numerically the transition between the viscosity and toughness dominated regimes and confirm the expressions based on scaling arguments of the transition time-scales in the two different directions.

2. Problem formulation

We focus our study on the case of a hydraulic fracture (HF) growing in a plane perpendicular to both the direction of the minimum horizontal in-situ stress σ_h and the material isotropy plane (see Fig. 1). We define the material canonical orthonormal basis $(\mathbf{e}_1, \mathbf{e}_2, \mathbf{e}_3)$ where $(\mathbf{e}_1, \mathbf{e}_2)$ defines the plane of material isotropy and \mathbf{e}_3 is the axis of rotational symmetry. In such a reference frame, the elastic stiffness tensor c_{ijkl} for a transversely isotropic (TI) material can be expressed in terms

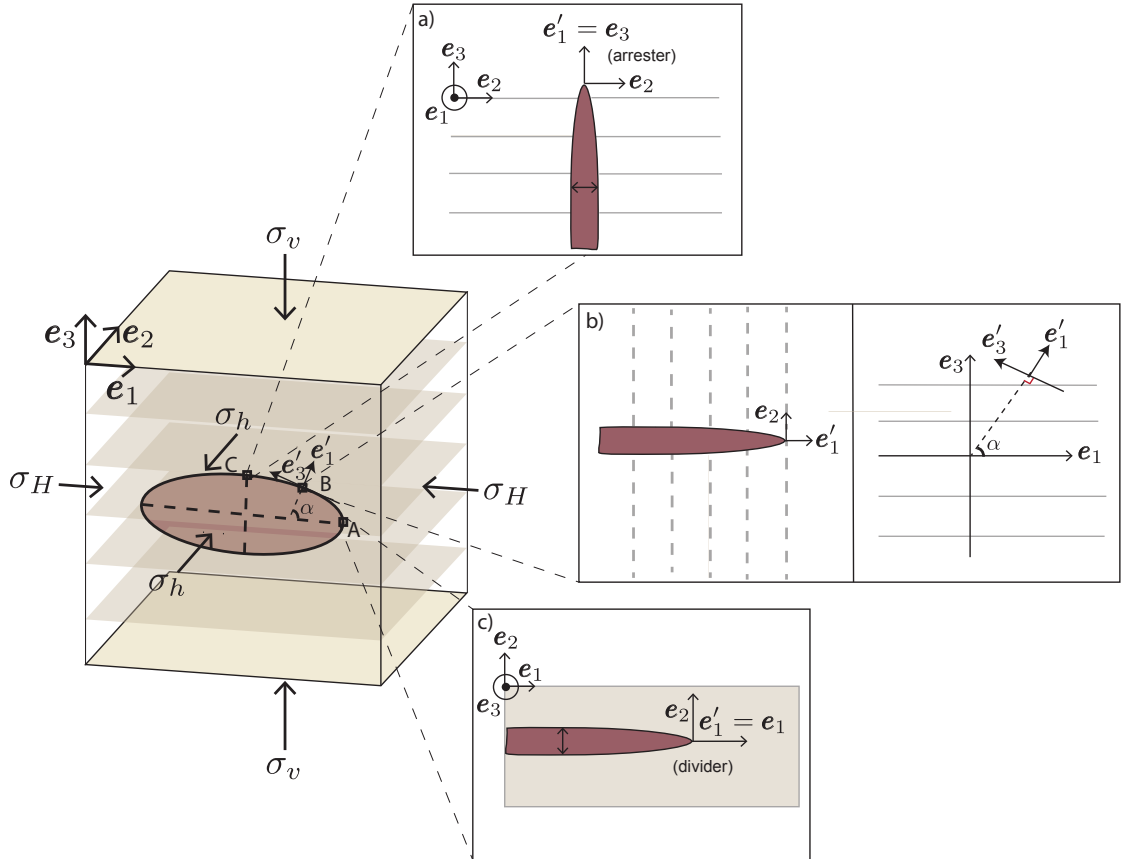


Figure 1: Schematic of a planar three dimensional hydraulic fracture growing perpendicular to the isotropy plane ($\mathbf{e}_1, \mathbf{e}_2$) and in the direction of the maximum horizontal stress σ_H . Different configurations of the near-tip region along the fracture front are also depicted: a) a semi-infinite fracture propagating along the direction perpendicular to the isotropy plane (arrested direction), b) a semi-infinite fracture propagating within the plane ($\mathbf{e}_1, \mathbf{e}_3$) at an angle α from \mathbf{e}_1 and c) a semi- infinite fracture propagating along the plane of isotropy (divider direction).

80 of five elastic parameters ($C_{11}, C_{12}, C_{13}, C_{33}, C_{44}$) using Voigt notation:

$$\begin{aligned} c_{ijkl} = & (C_{11} - 2C_{66})\delta_{ij}\delta_{kl} + C_{66}(\delta_{ik}\delta_{jl} + \delta_{il}\delta_{jk}) \\ & + (C_{11} + C_{33} - 2C_{13} - 4C_{44})\delta_{i3}\delta_{j3}\delta_{k3}\delta_{l3} \\ & + (C_{13} - C_{11} + 2C_{66})(\delta_{i3}\delta_{j3}\delta_{kl} + \delta_{k3}\delta_{l3}\delta_{ij}) \\ & + (C_{44} - C_{66})(\delta_{j3}\delta_{k3}\delta_{il} + \delta_{i3}\delta_{l3}\delta_{jk} + \delta_{j3}\delta_{l3}\delta_{ik} \\ & + \delta_{i3}\delta_{k3}\delta_{jl}) \end{aligned} \quad (1)$$

81 where $C_{66} = \frac{1}{2}(C_{11} - C_{12})$ and δ_{ij} denotes the Kronecker delta. We use the convention of summa-
82 tion on repeated indices.

83 Predictions of HF growth requires to couple linear elastic fracture mechanics with lubrication
84 flow inside the fracture (Detournay, 2016). The solution of such a moving boundary problem
85 consists in the time-evolution of the fracture contour, fracture width and fluid pressure inside the
86 fracture.

87 2.1. Elastic deformation

88 For a fracture propagating in an infinite medium, the quasi-static elastic problem can be re-
89 casted into a system of three boundary integral equations relating the traction vector $t_i = \sigma_{ij}n_j$
90 to the discontinuity of displacements d_i across the fracture. For a self-equilibrated fracture (with
91 continuity of tractions) of surface Σ and normal n_i (defined outward from its lower face), the
92 Somigliana representation for the elastic stress tensor $\sigma_{mn} = c_{mnkl}\epsilon_{kl}$ (ϵ_{kl} being the small-strain
93 tensor) can be written as (e.g. Bonnet, 1999; Mogilevskaya, 2014):

$$\sigma_{mn}(\mathbf{y}) = c_{mnkl}\epsilon_{kl}(\mathbf{y}) = -c_{mnkl} \int_{\Sigma} S_{ij}^k(\mathbf{y}, \mathbf{x}) \left(n_l(\mathbf{x}) \frac{\partial d_i}{\partial x_j}(\mathbf{x}) - n_j(\mathbf{x}) \frac{\partial d_i}{\partial x_l}(\mathbf{x}) \right) d\Sigma_{\mathbf{x}} \quad (2)$$

94 where $S_{ij}^k(\mathbf{y}, \mathbf{x})$ denotes the fundamental solution for the stress at point \mathbf{y} induced by a unit point
95 force at \mathbf{x} in a TI material (Pan and Chou, 1976). The induced traction vector $t_m = \sigma_{mn}(\mathbf{y})n_n(\mathbf{y})$
96 over the fracture surface Σ is thus given by:

$$t_m(\mathbf{y}) = -c_{mnkl}n_n(\mathbf{y}) \int_{\Sigma} S_{ij}^k(\mathbf{y}, \mathbf{x}) \left(n_l(\mathbf{x}) \frac{\partial d_i}{\partial x_j}(\mathbf{x}) - n_j(\mathbf{x}) \frac{\partial d_i}{\partial x_l}(\mathbf{x}) \right) d\Sigma_{\mathbf{x}} \quad (3)$$

97 It is worth noting that similarly to the case of an isotropic material, the shear and opening modes
98 uncouple for a planar fracture in the case of transverse isotropy (Lin and Keer, 1989; Keer and
99 Lin, 1990). In other words, a pure opening mode loading do not induce any shear displacement
100 discontinuity (and vice-versa). In the case of a planar hydraulic fracture (pure mode I fracture)
101 with a normal coinciding with the axis \mathbf{e}_2 of the material frame ($n_i = \delta_{i2}\mathbf{e}_2$) also being a direction
102 of the in-situ principal stress tensor, the quasi-static elastic problem reduces to a single boundary
103 integral equation for the opening mode:

$$p(\mathbf{y}) = p_f(\mathbf{y}) - \sigma_h = c_{22kl} \int_{\Sigma} S_{2j}^k(\mathbf{y}, \mathbf{x}) \left(\delta_{2l} \frac{\partial d_2}{\partial x_j}(\mathbf{x}) - \delta_{2j} \frac{\partial d_2}{\partial x_l}(\mathbf{x}) \right) dx_1 dx_3 \quad (4)$$

104 where the net pressure $p(\mathbf{y}) = p_f(\mathbf{y}) - \sigma_h$ controls the opening of the fracture. $p_f(\mathbf{y})$ is the fluid
105 pressure inside the fracture- which is neither uniform nor constant during propagation - and σ_h
106 is the in-situ minimum compressive horizontal stress (see Fig. 1). In the following, in line with
107 previous contributions, we write the fracture opening as $w(\mathbf{x}, t) = d_2(\mathbf{x}, t)$.

2.2. Fluid flow inside the fracture

Fluid flow inside the fracture follows lubrication theory (Batchelor, 1967). For an incompressible fluid and an impermeable surrounding rock, the width averaged mass conservation of the fluid inside the fracture reduces to

$$\frac{\partial w}{\partial t} + \frac{\partial q_i}{\partial x_i} = Q_o \delta(x_1, x_3) \quad i = 1 \& 3 \quad (5)$$

where Q_o denotes the constant fluid injection rate located at the origin. The width-averaged balance of momentum of the fluid inside the fracture reduces to Poiseuille's law, which relates the fluid flux $q_i = wv_i$ (where v_i is the 2D fluid velocity in the fracture plane - $i = 1 \& 3$ as per Fig. 1) to the fluid pressure gradient:

$$q_i(x_i) = -\frac{w^3}{\mu'} \frac{\partial p_f}{\partial x_i} \quad i = 1 \& 3 \quad (6)$$

where $\mu' = 12\mu$ is an effective viscosity used here to shorten notation.

2.3. Boundary conditions

For a hydraulic fracture propagating in an isotropic material, it can be shown that the fluid and fracture front coalesces when $\frac{\sigma_h K_{Ic}^2}{\mu' V E'_{iso}} \gg 1$ where V is the local front velocity, K_{Ic} the rock fracture toughness and E'_{iso} is the isotropic plane-strain modulus of the rock (Garagash and Detournay, 2000). An in-situ confining stress σ_h of the order of few $O(MPa)$ is sufficient to satisfy such a condition under most practical configurations. As a result, for a fracture propagating at depth, the fluid lag is negligible. The boundary conditions at the fracture front then reduce to (Detournay and Peirce, 2014)

$$w(\mathbf{x}_C, t) = 0, \quad q_i(\mathbf{x}_C, t)n_i(\mathbf{x}_C, t) = 0, \quad \mathbf{x}_C \in C(t).$$

2.4. Fracture Propagation condition

In the general case, the Irwin relation for the energy release rate per unit area of co-planar crack extension as function of the stress intensity factors K_i ($i = 1, 2, 3$) is given by (Barnett and Asaro, 1972; Rice, 1985):

$$\begin{aligned} G &= K_i \Lambda_{ij} K_j \quad i, j = 1, 2, 3 \\ \Lambda_{ij} &= \Lambda_{ji} \end{aligned} \quad (7)$$

where $\Lambda_{11} = \Lambda_{22} = 1/E'_{iso}$, $\Lambda_{33} = (1 + \nu)/E_{iso}$ for an isotropic material. However, the Irwin matrix Λ_{ij} is not necessarily diagonal for an anisotropic solid. It depends on the local direction of propagation and a matrix related to the pre-factor of the solution of an edge dislocation (Barnett and Asaro, 1972; Stroh, 1958) which is itself related to the point force Green's function S_{ij}^k . For general anisotropy and arbitrary direction of planar propagation, its expression can be obtained numerically (Barnett and Swager, 1971; Barnett and Asaro, 1972), or semi-explicitly in the material frame (Malén and Lothe, 1970).

In the configuration investigated here where the planar fracture is perpendicular to the isotropy plane of a transversely isotropic material (Fig. 1), the fracture mode decouples and as a result the Irwin matrix is diagonal. However, the expressions of Λ_{ii} remains function of the local propagation direction with respect to the material axis. For a planar fracture normal to \mathbf{e}_2 , it is solely function of the angle α between the normal to the local tangent to the fracture front C and the material axis \mathbf{e}_1 . For such a planar mode I fracture configuration, the local energy release rate along the front thus reduces to:

$$G(\alpha) = \frac{K_I^2}{E'_\alpha} \quad (8)$$

where $\Lambda_{11} = 1/E'_\alpha$. The exact expression of $E'_\alpha = E'(\alpha)$ is further derived in Section 3. The quasi-static linear elastic fracture mechanics propagation condition ($G = G_c$) can alternatively be written as the equality of the mode I stress intensity factor with the material fracture toughness K_{Ic} .

We will investigate the case where in addition to elastic transverse isotropy, the fracture toughness (or alternatively the critical fracture energy G_c) may also be anisotropic. In other words, the fracture toughness of the material may vary depending on the local fracture front propagation direction, i.e. as function of the angle α (Fig. 1). As a result, the propagation condition for a hydraulic fracture propagating under quasi-static equilibrium can be written as

$$K_I(\mathbf{x}_C, t) = K_{Ic}(\alpha), \quad \mathbf{x}_C \in C(t),$$

for all point \mathbf{x}_C along the fracture front C with a local propagation direction defined by the angle α .

In order to quantify the degree of anisotropy of fracture toughness, we use the ratio between the fracture toughness in the divider (\mathbf{e}_1) and arrester (\mathbf{e}_3) directions $\kappa = K_{Ic,1}/K_{Ic,3}$. The evolution of the material toughness can therefore be schematically expressed as:

$$K_{Ic}(\alpha) = K_{Ic,3} f(\alpha, \kappa) \quad (9)$$

where the dimensionless function f is obviously material dependent and must be characterized experimentally. In the following, we restrict to three limiting cases.

1. The case of a particular form of toughness anisotropy leading to an elliptical fracture shape under uniform loading (see Appendix A.1). Such a type of anisotropy will notably allow to verify our numerical model.
2. The case of an isotropic fracture toughness: $K_{Ic}(\alpha) = K_{Ic}$ (i.e. $\kappa = 1$, $f = 1$) such that according to (8) $G_c(\alpha) = K_{Ic}^2/E'_\alpha$.
3. The case of an isotropic fracture energy: $G_c(\alpha) = G_c$, which gives $K_{Ic}(\alpha) = \sqrt{G_c E'_\alpha}$ according to (8).

3. Near-tip elastic operator: expression for $\Lambda_{11} = 1/E'_\alpha$

We now derive an exact expression for the mode I compliance $\Lambda_{11} = 1/E'_\alpha$ appearing in the Irwin's matrix for a planar fracture perpendicular to the isotropy plane. Such a local near-tip elastic

constant (function of the propagation direction) is directly obtained by deriving the near-tip elastic operator for a mode I crack. The near-tip elastic configuration is akin to a 2D semi-infinite fracture where the out of plane direction is taken locally as the tangent to the fracture front. Such a direction is thus characterized by the angle α with respect to the horizontal axis \mathbf{e}_1 (divider direction). Three different local configurations are displayed in Fig. 1 for illustration.

This near-tip semi-infinite fracture problem is more easily described in a local system of coordinates $(\mathbf{e}'_1, \mathbf{e}'_2, \mathbf{e}'_3)$ where \mathbf{e}'_1 is the direction of propagation of the semi-infinite fracture with $(\widehat{\mathbf{e}'_1, \mathbf{e}_1}) \equiv \alpha$, and the normal to the fracture surface is $\mathbf{e}'_2 = \mathbf{e}_2$ and \mathbf{e}'_3 is an axis such that $(\mathbf{e}'_1, \mathbf{e}'_2, \mathbf{e}'_3)$ define a direct orthonormal basis. The change of coordinates between such a local frame and the global (material) frame $(\mathbf{e}_1, \mathbf{e}_2, \mathbf{e}_3)$ is given by:

$$\mathbf{e}'_i = P_{i'j} \mathbf{e}_j, \quad (10)$$

where $P_{i'j}$ is defined in the material canonical basis as

$$P_{i'j} = \begin{pmatrix} \cos(\alpha) & 0 & \sin(\alpha) \\ 0 & 1 & 0 \\ -\sin(\alpha) & 0 & \cos(\alpha) \end{pmatrix}$$

The elastic stiffness tensor c'_{ijkl} in such a local basis $(\mathbf{e}'_1, \mathbf{e}'_2, \mathbf{e}'_3)$ is related to c_{ijkl} (Eq. (2)) in the material basis as:

$$c'_{ijkl} = P_{i'j} P_{j'k} P_{k'l} P_{l'i} c_{ijkl} \quad (11)$$

Sufficiently close to the local, the planar fracture edge C has locally an infinite radius of curvature. Any variation of the fracture opening near the front occurs in the direction normal to the front and thus the surface gradient in the elastic integral equation (2) is reduced to be only along the local propagation direction \mathbf{e}'_1 . As a result, for such a semi-infinite fracture (with the tip located at the origin), the representation for the strain tensor is:

$$\epsilon_{k'l'}(\mathbf{y}') = \int_0^\infty S_{2j'}^{k'}(\mathbf{y}', \mathbf{x}') (\delta_{l'2} \delta_{j'1'} - \delta_{j'2} \delta_{l'1'}) \frac{\partial w}{\partial x'_1}(\mathbf{x}') dx'_1. \quad (12)$$

We directly verify from Eq. (12) that the local propagation occurs in state of plane-strain:

$$\epsilon_{1'3'}(\mathbf{y}') = \epsilon_{2'3'}(\mathbf{y}') = \epsilon_{3'3'}(\mathbf{y}') = 0$$

We can thus directly write the near-tip elastic relation from the plane elastic solution of an edge dislocation in an orthotropic solid (Hirth and Lothe, 1982). Using the distributed dislocation technique, the elastostatic boundary integral equation for such a tensile semi-infinite fracture takes the usual form of the Hilbert transform:

$$p_f(y'_1) - \sigma_h = \frac{E'_\alpha}{4\pi} \int_0^\infty \frac{1}{y'_1 - x'_1} \frac{\partial w}{\partial x'_1} dx'_1, \quad (13)$$

where $E'_\alpha = E'(\alpha)$ is a near-tip elastic modulus which depends on the angle of propagation of the semi-infinite fracture with respect to the material axis \mathbf{e}_1 and the different elastic constants. From the solution of Hirth and Lothe (1982) and the change of coordinates previously defined, we obtain

$$E'_\alpha = \frac{2 M(\alpha) C'_{22}(\alpha) C'_{66}(\alpha)}{\sqrt{C'_{22}(\alpha) C'_{11}(\alpha)}} \quad (14)$$

where $C'_{ij}(\alpha)$ are the stiffness coefficients (Eq.(11)) in Voigt notation in the local frame $(\mathbf{e}'_1, \mathbf{e}'_2, \mathbf{e}'_3)$ defined by α . M is a dimensionless elastic constant equal to:

$$M(\alpha) = \left(\sqrt{C'_{22}(\alpha)C'_{11}(\alpha)} + C'_{12}(\alpha) \right) \times \left(\frac{\sqrt{C'_{22}(\alpha)C'_{11}(\alpha)} - C'_{12}(\alpha)}{C'_{22}(\alpha)C'_{66}(\alpha) \left(\sqrt{C'_{22}(\alpha)C'_{11}(\alpha)} + C'_{12}(\alpha) + 2C'_{66}(\alpha) \right)} \right)^{1/2}.$$

The form of the integral operator (13) is exactly the same as the case of isotropy pending the expression of E'_α . As a result, we directly identify the coefficient of the Irwin relation (8) as $\Lambda_{11} = 1/E'_\alpha$.

3.1. Evolution of E'_α

The near-tip elastic modulus E'_α evolves monotonically with α (see Fig. 2) and satisfies:

$$E'_\alpha(\alpha) = E'_\alpha(\pi - \alpha) = E'_\alpha(\pi + \alpha) = E'_\alpha(-\alpha).$$

In case of elastic isotropy, it reduces to the isotropic plane-strain Young's modulus:

$$E'_{iso} = C_{11} \left(1 - \frac{C_{12}^2}{C_{11}^2} \right) \quad (15)$$

For $\alpha = 0$, the semi-infinite fracture propagates along the divider \mathbf{e}_1 direction (case Fig. 1)). The elastic modulus depends only on two elastic parameters C_{11} and C_{12} :

$$E'(\alpha = 0) = E'_\alpha(\alpha = 0) = E'_1 = \frac{C_{11}^2 - C_{12}^2}{C_{11}}.$$

On the other hand, when the semi-infinite fracture propagates in the arrester direction \mathbf{e}_3 ($\alpha = \pi/2$), E'_3 depends on four elastic parameters (see also Chertov (2012); Laubie and Ulm (2014)):

$$E'_\alpha \left(\alpha = \frac{\pi}{2} \right) = E'_3 = \frac{\sqrt{C_{33}/C_{11}}(-C_{13}^2 + C_{11}C_{33})}{C_{33} \sqrt{\frac{-C_{13}^2 - 2C_{13}C_{44} + C_{11}(C_{33} + 2\sqrt{C_{33}/C_{11}}C_{44})}{C_{11}C_{44}}}}.$$

It is interesting to write E'_α (14) as a product of a characteristic elastic modulus and a dimensionless function \mathcal{F} depending on four dimensionless elastic constant and the local angle of propagation α : $E'_\alpha = E'_* \mathcal{F}(\beta, \epsilon, \delta, C_{13}/C_{11}, \alpha)$. The characteristic elastic modulus E'_* can be chosen either as E'_1 , E'_3 , or any combination of C_{ij} . We take for illustration the average value of E'_1 and E'_3 . We also express the dimensionless function $\mathcal{F}(\beta, \epsilon, \delta, C_{13}/C_{11}, \alpha)$ as depending on relevant dimensionless elastic parameters such as the ratio $\beta = E'_1/E'_3$, the ratio C_{13}/C_{11} , and the Thomsen parameters (ϵ, δ) (Thomsen, 1986) defined as:

$$\epsilon = \frac{C_{11} - C_{33}}{2C_{33}} \quad \delta = \frac{(C_{13} + C_{44})^2 - (C_{33} - C_{44})^2}{2C_{33}(C_{33} - C_{44})} \quad (16)$$

Material	$\beta = E'_1/E'_3$	ϵ	δ	C_{13}/C_{11}
Olkiluoto mica gneiss (Hakala et al., 2007)	1.16	0.18	0.09	0.26
Gas-saturated Shaly Coal (Wang, 2002)	1.26	0.51	-0.17	0.06
Woodford53 shale (Laubie, 2013)	1.31	0.31	0.14	0.29
Opalinus Clay (Thöny, 2014)	1.33	0.5	0.49	0.67
Yeocheon schist (Cho et al., 2012)	1.43	1.15	1.23	0.22
Calcareous mudstone (Chertov, 2012)	1.9	0.78	0.66	0.44

Table 2: Dimensionless elastic parameters values corresponding to the different rocks given in Table 1.

208 Finally, we can re-express the near-tip elastic modulus E'_α in the following form:

$$E'_\alpha = \langle E' \rangle \times \mathcal{F}(\beta = E'_1/E'_3, \epsilon, \delta, C_{13}/C_{11}, \alpha) \quad (17)$$

$$\langle E' \rangle = (E'_1 + E'_3)/2 \quad (18)$$

209 For most rocks, the Thomsen parameters ranges from 0 to 1, the ratio $\beta = E'_1/E'_3$ varies between 1
210 and 2 (weak to strong anisotropy) while C_{13}/C_{11} is usually smaller than 1 (see Table 2. We display
211 in Fig. 2 the scaled modulus $E'_\alpha/\langle E' \rangle$ as a function of α for different values of the dimensionless
212 elastic parameters ($\beta, \epsilon, \delta, C_{13}/C_{11}$) in the range expected for rocks. We also compare the analyt-
213 ical expression $E'_\alpha/\langle E' \rangle$ (Eq. (14)) in solid line with an approximation $E'_{app}/\langle E' \rangle$ put forward by
214 Laubie and Ulm (2014) in dashed line, where E'_{app} is given by:

$$\frac{1}{E'_{app}} = \frac{\cos^2(\alpha)}{E'_1} + \frac{\sin^2(\alpha)}{E'_3} \quad (19)$$

215 Such an approximated expression for the local near-tip elastic modulus depends only on β (not on
216 ϵ, δ and C_{13}/C_{11}). As can be observed from Fig. 2, the magnitude of the difference in the elastic
217 modulus depends on the ratio β whereas the evolution is function of the other dimensionless elastic
218 parameters ($\beta, \delta, \epsilon, C_{13}/C_{11}$). The transition from E'_1 to E'_3 is steeper for increasing (β, δ), and for
219 decreasing ($\epsilon, C_{13}/C_{11}$). We observe that the approximation (19) always provides a lower estimate
220 of the exact E'_α . This approximation is only accurate for weak anisotropy ($\beta < 1.2$) and departs
221 significantly from the exact value for smaller values of C_{13}/C_{11} , ϵ , and larger δ, β respectively.

222 4. Near-tip hydraulic fracture asymptotes for a transversely isotropic material

223 As a direct consequence of the fact that the near-tip elastic operator (13) has a form strictly
224 similar than the isotropic case pending the use of the proper near-tip elastic modulus E'_α (14),
225 the known asymptotic solutions for a steadily moving semi-infinite HF in an isotropic material
226 (Desroches et al., 1994; Garagash et al., 2011) can be directly transposed to the transversely
227 isotropic case.

228 For a steadily moving HF with velocity V , the linear elastic fracture mechanics (LEFM) asymp-
229 tote prevails in the near-field. The fracture width follow the classical square-root evolution

$$w(x'_1) = \sqrt{32/\pi} \frac{K_{Ic}(\alpha)}{E'_\alpha} \sqrt{x'_1}, \quad x'_1 \ll \ell_{mk}^\infty. \quad (20)$$

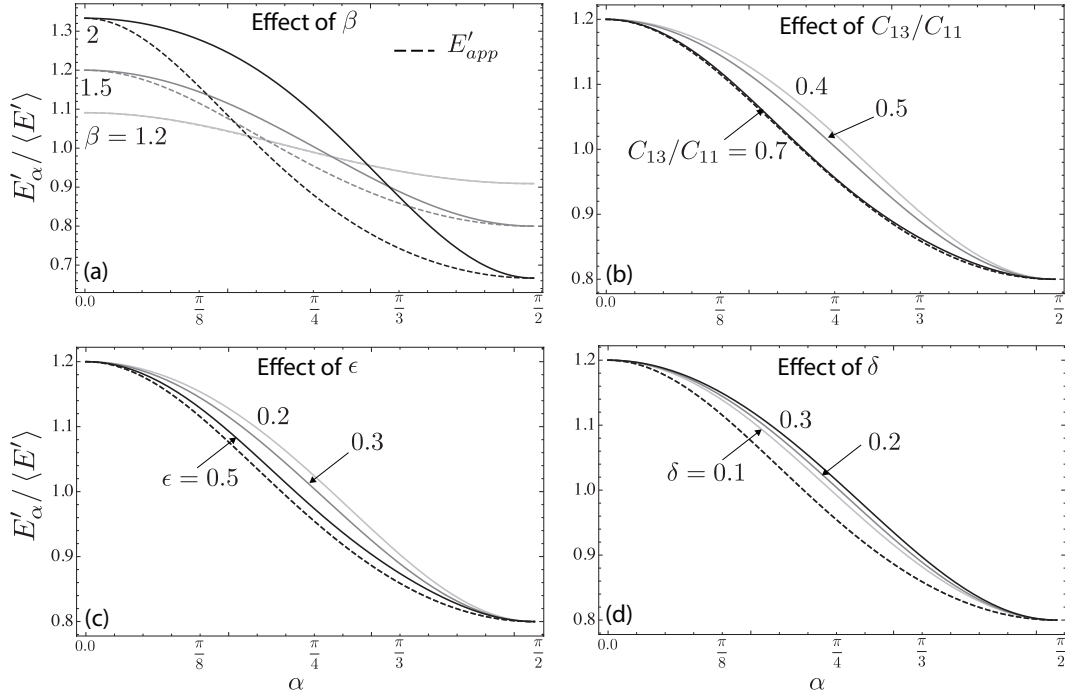


Figure 2: Near-tip elastic modulus as function of α using the exact solution (Eq. (14) - solid line) and its approximation (Eq. (19) dashed line). Reference values: $\beta = 1.5$, $C_{13}/C_{11} = 0.5$, $\epsilon = 0.3$ and $\delta = 0.2$ (black lines). (a) Effect of $\beta = (1.2, 1.5, 2)$, (b) effect of $C_{13}/C_{11} = (0.4, 0.5, 0.7)$, (c) effect of $\epsilon = (0.2, 0.3, 0.5)$, and (d) effect of $\delta = (0.1, 0.2, 0.3)$.

where E'_α is the near-tip TI elastic modulus (14) and $K_{Ic}(\alpha)$ is the corresponding value of toughness. On the other hand, in the far-field, the solution is dominated by viscous flow. The so-called viscous dominated asymptote for fracture width is given by (Desroches et al., 1994):

$$w(x'_1) = 2^{1/3} 3^{5/6} \left(\frac{\mu'}{E'_\alpha} V \right)^{1/3} x_1'^{2/3}, \quad x_1' \gg \ell_{mk}^\infty. \quad (21)$$

The transition between the near-tip LEFM and the far-field viscosity asymptotes is governed by the characteristic lengthscale ℓ_{mk}^∞ defined as the distance where the width given by two asymptotes are of the same order of magnitude (Garagash et al., 2011):

$$\ell_{mk}^\infty = \frac{K'^6}{E_\alpha'^4 V^2 \mu'^2}, \quad (22)$$

where $K' = \sqrt{\frac{32}{\pi}} K_{Ic}$. The solution for the complete transition between the toughness and viscous asymptote can be found in Garagash et al. (2011).

5. Numerical solution

We resort to numerical modeling using the implicit level set algorithm (ILSA) to study the growth of a planar 3D hydraulic fracture in a transversely isotropic medium under the configuration depicted in Fig. 1. We refer to Peirce and Detournay (2008); Peirce (2015); Dontsov and

Peirce (2017) for details of the scheme originally developed for the isotropic case and to Zia and Lecampion (2019) for its python implementation. We discuss here briefly this scheme emphasizing the extensions required to account for transverse isotropy.

The fracture plane is discretized using a Cartesian grid consisting of uniform rectangular elements. We discretize the elasticity equation (4) using a collocation method based on rectangular displacement discontinuity elements. The solution for a rectangular displacement discontinuity in a TI medium can be found in Pan et al. (2014). The fracture width is thus constant over an element and the fluid pressure is evaluated at the element center. The lubrication flow is discretized spatially with a five-point stencils finite difference scheme and with a backward Euler (implicit) scheme for time integration. The resulting non-linear hydro-mechanical system (elasticity and lubrication) is solved using fixed point iterations for a given position of the fracture front.

A level set function $\phi(x_1, x_3)$ is used to represent the fracture front located in the $(\mathbf{e}_1, \mathbf{e}_3)$ plane. The propagation algorithm relies on the coupling of the finite discretization with the near-tip solution of a steadily moving HF (see section 4) in the rim of elements near the front. The fracture front is advanced over a time-step through an iterative procedure (until subsequent estimations of the level set falls below a fixed tolerance, set to 10^{-3} here). For a given position of the front, the non-linear hydro-mechanical system is solved. The new trial width in the elements located just before the tip elements (ribbon elements) are used to invert the near-tip solution and obtain the new shortest distance to the fracture front (from the ribbon elements centers). The Eikonal equation is then solved to update the level set function from the tip region outward to the rest of the yet unfractured domain using the fast marching method. The front is then reconstructed in a piece-wise manner and the asymptotic solution enforced in a weak sense in the tip elements (see Peirce (2015) for more details). In the case of a transversely isotropic material, the difference with the isotropic case stems (beside the elastic operator) from the fact that the complete near-tip HF solution (spanning the transition from the toughness to the viscosity asymptote) depends on the local propagation direction (via the dependence of E'_α and K_{Ic} on the angle α) beside the local front velocity. This introduces another non-linearity which is solved by iterating on the local propagation direction: by repeatably inverting the tip asymptote and reconstructing new estimate of the front until convergence (Zia et al., 2018). It is worth noting that the local propagation direction (local normal to the front) can be directly obtained from the gradient of the level set function $n_i = \phi_{,i}/\|\phi_{,i}\|$ in the ribbon element. It is then straightforward to estimate its angle α with the \mathbf{e}_1 axis and the corresponding near-tip elastic modulus (14) and toughness (9). A tolerance of 10^{-3} has been used to check the convergence of the local propagation direction in all simulations reported here.

6. Scaling and structure of the solution

Our aim is to study how the geometry of the HF deviates from a radial shape due to material isotropy. We thus follow the scaling first introduced by Savitski and Detournay (2002) for the case of a radial hydraulic fracture driven by a Newtonian fluid in an isotropic medium. A characteristic length scale $L(t)$ scales all distances, while the fracture width and pressure are scaled by $W(t)$ and $P(t)$ respectively. We define a normalized fracture contour γ , fracture opening Ω and net pressure

Π as:

$$C(t) = L(t)\gamma(\mathcal{P}(t), \beta, \epsilon, \delta, C_{13}/C_{11}, \kappa, f(\alpha, \kappa)) \quad (23)$$

$$w(x_1, x_3, t) = W(t)\Omega(x_1/L(t), x_3/L(t), \mathcal{P}(t), \beta, \epsilon, \delta, C_{13}/C_{11}, \kappa, f(\alpha, \kappa)) \quad (24)$$

$$p(x_1, x_3, t) = P(t)\Pi(x_1/L(t), x_3/L(t), \mathcal{P}(t), \beta, \epsilon, \delta, C_{13}/C_{11}, \kappa, f(\alpha, \kappa)) \quad (25)$$

where for transverse isotropy in addition to the evolution parameter $\mathcal{P}(t)$, the solution also depends on the dimensionless elastic parameters previously defined and the ratio of toughness and its evolution function. Following the isotropic case for a radial fracture (Savitski and Detournay, 2002), two different scalings can be obtained either emphasizing the importance of energy dissipation in viscous flow (so-called M/viscosity scaling) or in the creation of new fracture surfaces (K/toughness scaling). The corresponding lengthscales and the associated dimensionless parameter \mathcal{P} governing the solution in both scaling are recalled in Table 3. We have written them here as function of a characteristic elastic modulus E'_* and a characteristic toughness K'_* . The viscosity dominated propagation regime (M-scaling) is valid at early time of growth. This can be grasped from Table 3 where we can see that the dimensionless toughness \mathcal{K} increases with time (and is directly related to the dimensionless viscosity $\mathcal{M} = \mathcal{K}^{-18/5}$ which decreases with time). At very early time, fracture toughness is irrelevant ($\mathcal{K} \sim 0$) and fracture growth is propagating in the so-called viscosity dominated regime where the solution is self-similar for radial growth (given by the characteristic scales and solution for the dimensionless length, pressure and opening in viscosity scaling all of order 1). At large time, on the contrary, fracture toughness dominates the energy dissipation and viscous flow becomes irrelevant. The fracture propagates in the viscosity dominated regime where the solution is also self-similar. The transition between these two regimes (viscosity to toughness) is captured by the characteristic timescale t_{mk} :

$$t_{mk} = \left(\frac{\mu'^5 E'^{13}_* Q_o^3}{K'^{18}_*} \right)^{1/2}. \quad (26)$$

at which $\mathcal{K}(t_{mk}) = \mathcal{M}(t_{mk})$ (or alternatively $L_m(t_{mk}) = L_k(t_{mk})$). A corresponding (M-K) scaling can then be used where the characteristic scales are not independent of time, and the solution only depends on t/t_{mk} .

For the case of a transversely isotropic material, several choices can be made for the characteristic modulus and toughness. In view of the configuration investigated here, we take values along the divider direction (\mathbf{e}_1) and the arrester direction (\mathbf{e}_3). The solution will now be function, in addition to a dimensionless time (e.g. $t/t_{mk,*}$), on the ratio between the dimensionless toughness (or viscosity) between the arrester and the divider directions. This is similar to taking the ratio of the transition time-scales between the arrester and divider directions. Such a ratio is solely function of the ratio of toughness $\kappa = K_{Ic,1}/K_{Ic,3}$ and plane strain elastic modulus $\beta = E'_1/E'_3$:

$$\frac{t_{mk,3}}{t_{mk,1}} = \left(\frac{\mathcal{K}_1}{\mathcal{K}_3} \right)^9 = \beta^{-13/2} \kappa^9 \quad (27)$$

We see that a small anisotropy of toughness and elasticity (e.g. $\beta = \kappa^{-1} = 1.2$) induces a strong anisotropy in the transition from viscosity to toughness between the divider and the arrester direction ($t_{mk,1}/t_{mk,3} \approx 17$). The fracture front will likely reaches the toughness propagation regime earlier in the arrester direction for these particular values of β and κ .

	Viscosity (M)	Toughness (K)	Viscosity to toughness (M-K)
$L(t)$	$L_m = \left(\frac{E'_* Q_o^3 t^4}{\mu'} \right)^{1/9}$	$L_k = \left(\frac{E'_* Q_o t}{K'_*} \right)^{2/5}$	$L_{mk} = \frac{\mu' Q_o E'_*{}^3}{K'_*{}^4}$
$W(t)$	$W_m = \left(\frac{Q_o^3 \mu'^2 t}{E'_*{}^2} \right)^{1/9}$	$W_K = \left(\frac{Q_o K'_*{}^4 t}{E'_*{}^4} \right)^{1/5}$	$W_{mk} = \left(\frac{\mu' Q_o E'_*}{K'_*{}^2} \right)^{1/2}$
$P(t)$	$P_m = \left(\frac{\mu' E'_*{}^2}{t} \right)^{1/3}$	$P_k = \left(\frac{K'_*{}^6}{Q_o E'_* t} \right)^{1/5}$	$P_{mk} = \left(\frac{K'_*{}^{18}}{Q_o^3 E'_*{}^9 \mu'} \right)^{1/6}$
$\mathcal{P}(t)$	$\mathcal{K} = K'_* \left(\frac{t^2}{\mu'^5 Q_o^3 E'_*{}^{13}} \right)^{1/18}$	$\mathcal{K} = 1$	$\mathcal{K} = \left(\frac{t}{t_{mk}} \right)^{1/9}$
$\mathcal{P}(t)$	$\mathcal{M} = 1$	$\mathcal{M} = \mu' \left(\frac{Q_o^3 E'_*{}^{13}}{K'_*{}^{18} t^2} \right)^{1/5}$	$\mathcal{M} = \left(\frac{t_{mk}}{t} \right)^{2/5}$

Table 3: Characteristic scales and dimensionless parameters in the viscosity (M), toughness (K) and the transition from viscosity to toughness (M-K). Note that $\mathcal{M} = \mathcal{K}^{-18/5}$.

The ratio of timescales $t_{mk,3}/t_{mk,1}$ likely captures the main effect of transverse anisotropy on HF growth, but the Thomsen parameters ϵ , δ as well as C_{13}/C_{11} and the details of the toughness evolution function $f(\alpha, \kappa)$ also affect the solution. The fracture shape will also evolve between the early time (viscous dominated) and toughness dominated regime. We quantify these effects numerically in what follows.

Unless otherwise specified, we scale the numerical results with the average value of the plane strain elastic modulus $E'_* = \langle E' \rangle = (E'_1 + E'_3)/2$ and the average toughness $K'_* = \langle K' \rangle = (K'_1 + K'_3)/2$. We will also refer the half-lengths in the divider (\mathbf{e}_1) and arrester (\mathbf{e}_3) directions as a and b respectively, and denote abusively the fracture aspect ratio as b/a although the fracture shape is not necessarily elliptical.

7. Viscosity dominated propagation

We first focus on the viscosity dominated regime which corresponds to early time (e.g. $t < t_{mk}$ in the tougher direction). In such a regime, the solution is not affected by fracture toughness (see the scaling in Table 3). The interest therefore lies in the effect of TI elasticity on the potential deviation of the fracture from the radial geometry obtained for isotropic material. We investigate the effect of the dimensionless elastic parameters β , ϵ , δ and C_{13}/C_{11} by varying them around the set of base values already used to illustrate the variation of the near-tip modulus (see Fig. 2).

In all the simulations, the fracture plane is discretized with 100×100 rectangular element ($\Delta x_1 = 2\Delta x_3$). Our numerical scheme use a re-meshing strategy (ensuring volume conservation). The discretization is coarsened by a factor when the fracture reaches the end of the grid. This allow us to span multiple time and length scales at a reasonable cost. The fracture is initialized as a small radial fracture with a fluid pressure slightly above the minimum confining stress σ_h .

The evolution of the dimensionless major and minor semi-axis $a(t)$ and $b(t)$ and the dimensionless width at the injection with time are displayed in Fig. 3 for different values of $\beta = E'_1/E'_3$.

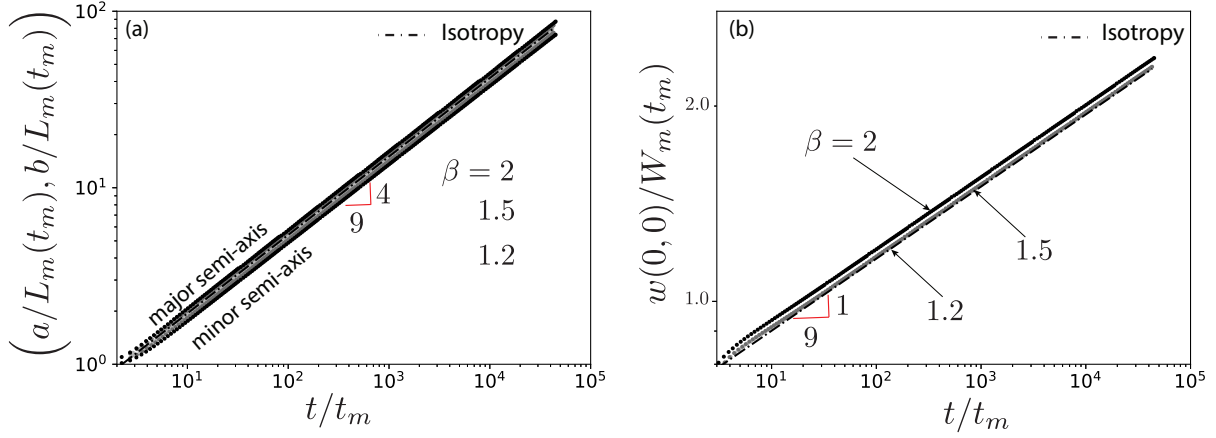


Figure 3: Viscosity dominated propagation: time evolution of the dimensionless major $a(t)/L_m(t_m)$ and minor $b(t)/L_m(t_m)$ semi axis in (a), and of the dimensionless width at the injection point $w(0,0)/W_m(t_m)$ in (b). The numerical simulations are performed for different values of $\beta = (1.2, 1.5, 2)$ with $\epsilon = 0.3$, $\delta = 0.2$, and $C_{13}/C_{11} = 0.5$.

The other dimensionless elastic parameters ϵ , δ and C_{13}/C_{11} have almost no effect on the solution in that propagation regime (see Figs.3-5). The time in these plots is scaled using a timescale t_m corresponding to the time taken to reach a fracture lengthscale of 1 m: $L_m(t_m) = 1$. Similarly, the width $w(t)$, the semi-axis $a(t)$ and $b(t)$ are scaled by $W_m(t_m)$ and $L_m(t_m)$ respectively. The results for an isotropic material are also displayed (in dot-dashed line) for reference.

Fig. 3 clearly shows the self similarity of the solution in the viscosity dominated regime. It follows the same power law of time as in the isotropic case: $4/9$ for the radius, and $1/9$ for width. The difference of the fracture semi-axes with the isotropic radial case ($b(t)/a(t) = 1$) is barely visible in such log-log plots, similarly for the width at the injection point - except for $\beta = 2$ (Fig. 3b)). As the solution is self-similar in this viscosity dominated regime, we can plot the dimensionless fracture footprint (removing the time-dependence contained in $L_m(t)$) γ_m for different set of parameters in Fig. 4 (we plot a quarter of the fracture shape due to symmetry), while the corresponding dimensionless profiles of width and pressure along the major axis \mathbf{e}_1 are exhibited in Figs. 5 and 6 respectively.

An elongation of the fracture in the divider direction (\mathbf{e}_1) for increasing β can be observed from the dimensionless self-similar footprint (Fig. 4). The other elastic constants do not appear to influence the solution significantly. A difference of 18% between the fracture height and length is obtained for $\beta = 2$. The evolution of the fracture aspect ratio as function of β can be well approximated as $b/a \approx 0.76\beta^{-1/3}$ (see Fig.4a-inset). Such a variation of b/a with β can be actually be easily recovered analytically from the near-tip solution as discussed in Bessmertnykh and Dontsov (2018). Matching the width given by the viscosity asymptote Eq. (21) in both the arrester and divider directions gives $a^{2/3}/E_1'^{1/3} \left(\frac{da}{dt}\right)^{1/3} \propto b^{2/3}/E_3'^{1/3} \left(\frac{db}{dt}\right)^{1/3}$, where $\frac{da}{dt}$ and $\frac{db}{dt}$ are the propagation velocities of the crack tips at the major and the minor axes respectively. Assuming a self-similar growth, the ratio of the these tip velocities should be constant as shown in Bessmertnykh and

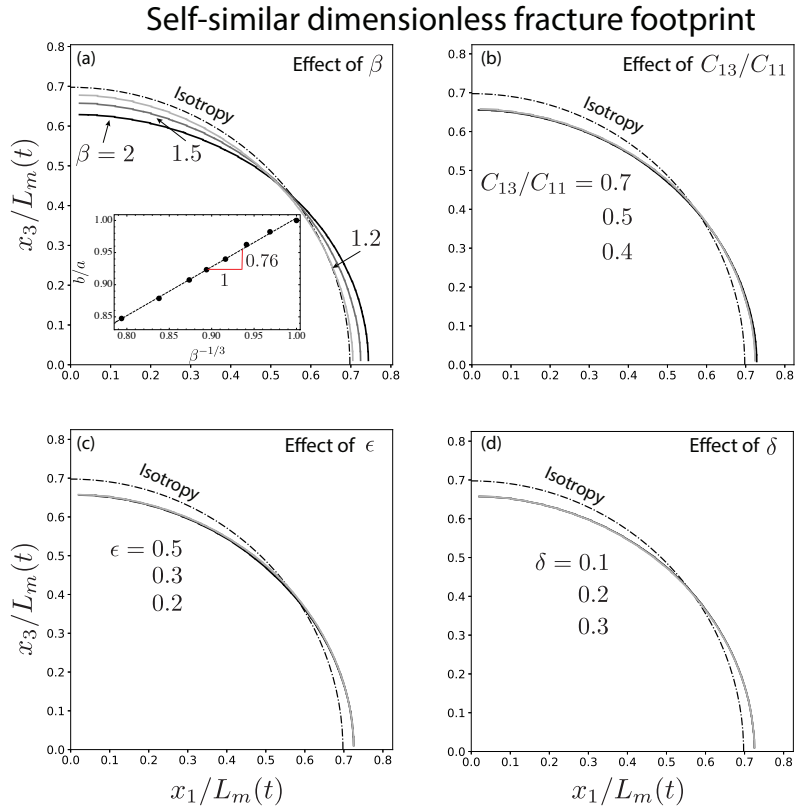


Figure 4: Viscosity dominated propagation - self similar fracture footprint γ_m (quarter of the footprint). Reference parameters: $\beta = 1.5$, $C_{13}/C_{11} = 0.5$, $\epsilon = 0.3$, and $\delta = 0.2$. Effect of the variations of: (a) $\beta = (1.2, 1.5, 2)$, (b) $C_{13}/C_{11} = (0.4, 0.5, 0.7)$, (c) $\epsilon = (0.2, 0.3, 0.5)$, and (d) $\delta = (0.1, 0.2, 0.3)$. The inset in figure (a) displays the evolution of the fracture aspect ratio b/a as function of β .

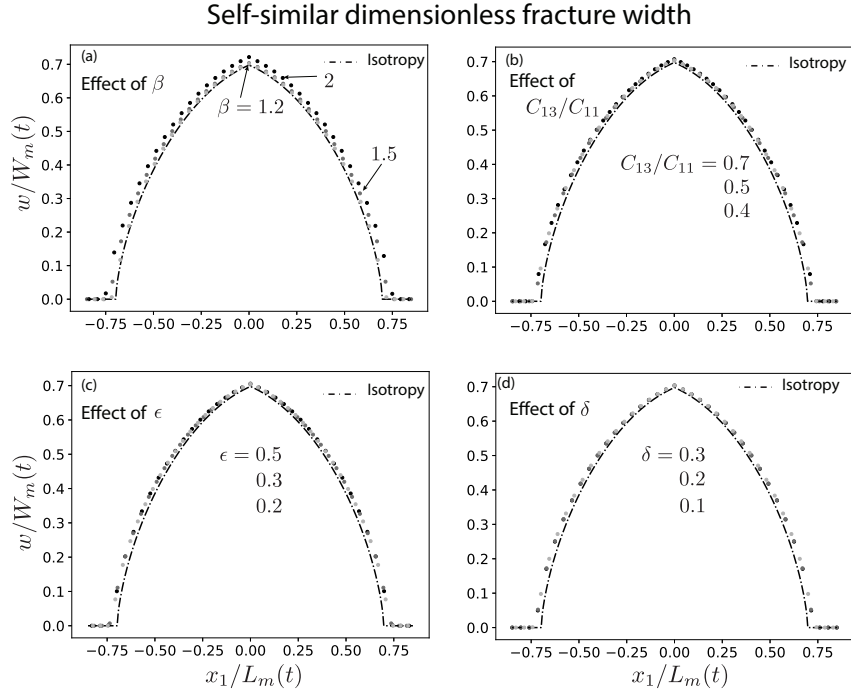


Figure 5: Viscosity dominated regime - self similar width profiles $w/W_m(t)$ along the major axis \mathbf{e}_1 . Reference parameters: $\beta = 1.5$, $C_{13}/C_{11} = 0.5$, $\epsilon = 0.3$, and $\delta = 0.2$ as base reference values. Effect of the variations of: (a) $\beta = (1.2, 1.5, 2)$, (b) $C_{13}/C_{11} = (0.4, 0.5, 0.7)$, (c) $\epsilon = (0.2, 0.3, 0.5)$, and (d) $\delta = (0.1, 0.2, 0.3)$.

Dontsov (2018):

$$\frac{db}{da} = \frac{b}{a} \quad (28)$$

As a result, we recover the evolution of the aspect ratio with β : $b/a \propto (E'_3/E'_1)^{1/3} = \beta^{-1/3}$.

The fracture width and pressure have similar evolution along the minor and major axis (\mathbf{e}_3 and \mathbf{e}_1) actually very close to the isotropic solution. Figures 5 and 6 display the dimensionless width and net pressure profile along the major axis. The fracture width increases slightly with β , while it does not appear to be influenced by ϵ , δ and C_{13}/C_{11} .

8. Toughness dominated propagation

We now turn to the toughness dominated propagation regime, valid at large time compared to t_{mk} ($t \gg t_{mk}$). In this regime, viscous flow is negligible and has no effect on the solution: the pressure is uniform (but not constant) inside the fracture. We study here the combined effect of the anisotropy of elasticity and fracture toughness.

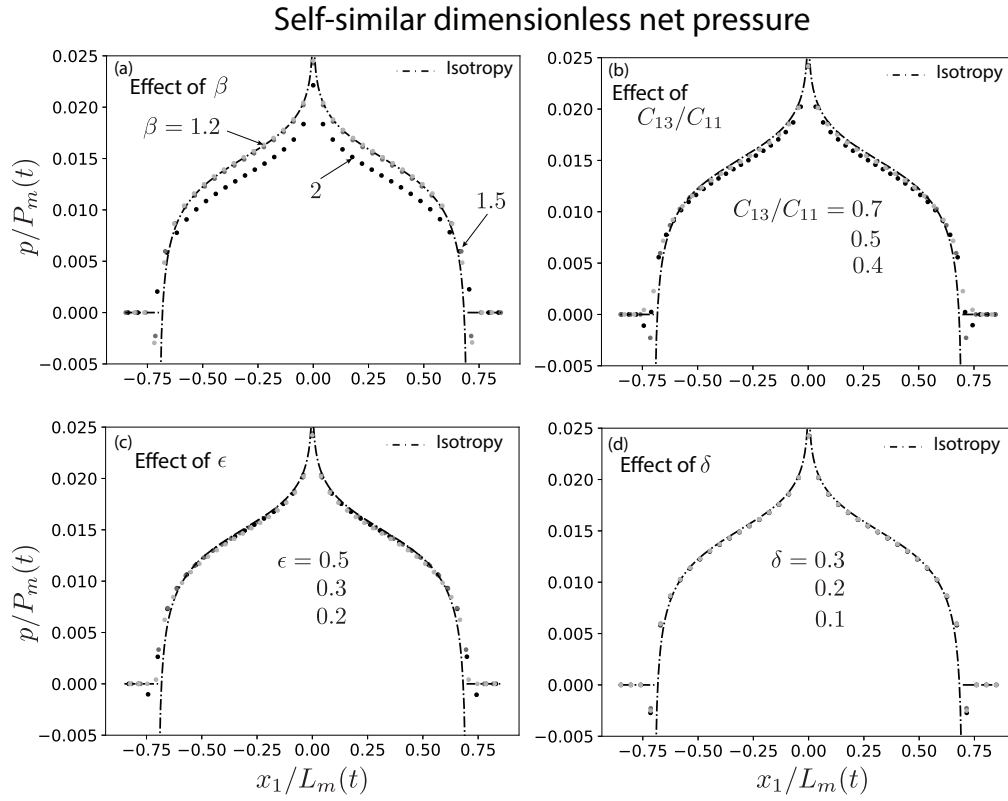


Figure 6: Viscosity dominated regime - self similar pressure profiles $p/P_m(t)$ along the major axis \mathbf{e}_1 . Reference parameters: $\beta = 1.5$, $C_{13}/C_{11} = 0.5$, $\epsilon = 0.3$, and $\delta = 0.2$ as base reference values. Effect of the variations of: (a) $\beta = (1.2, 1.5, 2)$, (b) $C_{13}/C_{11} = (0.4, 0.5, 0.7)$, (c) $\epsilon = (0.2, 0.3, 0.5)$, and (d) $\delta = (0.1, 0.2, 0.3)$.

8.1. Elliptical hydraulic fracture

We first investigate the case of a peculiar form of toughness anisotropy ensuring an exact elliptical shape under uniform loading:

$$K_{Ic} = K_{Ic,3} \left(\frac{E'_\alpha}{E'_3} \right) \left(\sin^2 \theta + \left(\frac{b}{a} \right)^2 \cos^2 \theta \right)^{1/4} \quad (29)$$

$$\theta = \arctan \left(\frac{b \tan \alpha}{a} \right) \quad (30)$$

Such a toughness evolution directly comes from the solution of the mode I stress intensity factor along the front of an uniformly pressurized elliptical crack in TI medium (see Appendix A). From such an elastic solution, it is then possible to obtain a solution for the propagation of such an elliptical hydraulic fracture in the toughness dominated regime. The details of such an analytical (and self-similar) HF propagation solution are given in Appendix A. It is worth noting that the HF propagates in a self similar manner with the same power law of time as in the isotropic case: $2/5$ for the radius, $1/5$ for width and $-1/5$ for the pressure.

Making use of Eq. (29) at $\alpha = \theta = 0$ (the divider direction) where $K_{Ic} = K_{Ic,1}$ and at $\alpha = \theta = \pi/2$ (the arrester direction) where $K_{Ic} = K_{Ic,3}$, we obtain the following relation between the ellipse aspect ratio and the ratio $K_{Ic,1}/K_{Ic,3}$:

$$\frac{b}{a} = \left(\frac{K_{Ic,1} E'_3}{K_{Ic,3} E'_1} \right)^2 = \left(\frac{\kappa}{\beta} \right)^2. \quad (31)$$

We use the fracture toughness function (29) in our numerical solver for the case $\kappa^{-1} = \beta = 1.2$. The resulting effect of anisotropy of elasticity and toughness are cumulative in that case (see Eq. (31) for $\kappa < 1$ and $\beta > 1$) and the corresponding aspect ratio is $b(t)/a(t) = 0.47$. We set the other elastic parameters to: $\epsilon = 0.3$, $\delta = 0.2$, and $C_{13}/C_{11} = 0.5$. The fracture is initialized with the analytical (isotropic) solution of a radial fracture propagating in toughness dominated regime. The rectangular domain is divided into 150 cells along \mathbf{e}_1 and 100 along \mathbf{e}_3 .

The numerical (black dots) and the analytical elliptical (green solid line) HF toughness dominated solutions are both displayed on Fig. 7. We scale the time in Figs. 7c, d, e and f by t_k defined as $L_k(t_k) = 1$, the pressure by $P_k(t_k)$, the width by $W_k(t_k)$ and semi-axis by $L_k(t_k)(=1)$. The analytical toughness dominated solution for isotropic toughness ($\kappa = 1$) and elasticity ($\beta = 1$) is also reported in Fig. 7 (dash-dotted lines) taking $E'_* = \langle E' \rangle$, and $K'_* = \langle K' \rangle$ as corresponding isotropic parameters. We clearly see that our numerical solution closely matches the analytical elliptical HF solution for both width profiles, major and minor axis as well as net pressure evolution. The relative error between the numerical results and the analytical solution of the major and minor axis always remain under five percent for about four decades of time - with only small oscillations associated with remeshing. It is worth to recall that the fracture is initialized as a radial following the isotropic solution. Interestingly, the width at the center $w/W_k(t_k)$ and the net pressure $p/P_k(t_k)$ takes slightly more time to converge toward the elliptical HF toughness solution (Figs. 7e and f) compared to the fracture shape (Figs. 7c).

This comparison verify our numerical solver, and has proven useful to test its robustness as anisotropy increases. It is also important to re-emphasize that the fracture has exactly an elliptical shape only for the evolution of fracture toughness given by Eq. (29).

8.2. Isotropic toughness

We now investigate the case of an isotropic fracture toughness: $K_{Ic}(\alpha) = K_{Ic}(\kappa = 1)$. We vary the different elastic parameters around the same set of reference values as before: $\beta = 1.5$, $\epsilon = 0.3$, $\delta = 0.2$, and $C_{13}/C_{11} = 0.5$. The numerical results for the self similar footprint γ_k and width profiles w/W_k along the major and the minor axis \mathbf{e}_1 and \mathbf{e}_3 are displayed in Figs. 8 and 9 respectively, whereas the pressure at the injection function of time is performed in Fig. 10. We use the toughness scaling defined in Table 3.

The fracture elongates more in the stiffer direction (\mathbf{e}_1) as can be seen from Fig. 8a. More importantly, the fracture is not elliptical. The fracture aspect ratio is proportional to β^{-2} as shown in Fig. 8a-inset. This is also the case for the elliptical fracture ($b/a = \beta^{-2}$ when $K_{Ic,1} = K_{Ic,3}$ in Eq. (31)). However, for isotropic toughness the slope is slightly different: $b/a \approx 0.9\beta^{-2}$. This implies that assuming an elliptical shape for the case of an isotropic toughness will underestimate the fracture aspect ratio by about 10%. Similarly than for the viscosity dominated regime, the relation between the fracture aspect ratio and β can be recovered from the toughness near-tip asymptote (20). Similarly to Bessmertnykh and Dontsov (2018), matching the width along the minor and major axis direction from the near-tip asymptote gives $\sqrt{b/a} \propto \frac{E'_3}{E'_1}$, in other words $b/a \propto \beta^{-2}$.

We also report in Fig. 8 the numerical results obtained using $E'_{app}(\alpha)$ as the near-tip elastic modulus. As previously discussed, for large β , the approximate solution E'_{app} underestimates the elastic near-tip modulus compared to the exact expression E'_α (Fig. 2-a). As a result, the computed fracture aspect ratio is also underestimated. As an illustration for $\beta = 2$, the ratio of the minor to major axis obtained using E'_{app} is equal to 0.32, whereas it is of 0.59 when using the exact near-tip elastic modulus E'_α . The difference between the fracture footprint obtained using either the exact E'_α and E'_{app} is however not very significant for $\beta \leq 1.5$. In other words, E'_{app} provides a good approximation only for weak anisotropy.

Figs. 8b and c display the fracture footprint for different C_{13}/C_{11} and ϵ respectively. These two elastic dimensionless parameters have the same effect on the behavior of the fracture footprint, i.e the aspect ratio increases from $b/a \approx 0.48$ for small value of C_{13}/C_{11} ($C_{13}/C_{11} = 0.4$) or ϵ ($\epsilon = 0.2$) to $b/a \approx 0.52$ for larger value of C_{13}/C_{11} ($C_{13}/C_{11} = 0.7$) or ϵ ($\epsilon = 0.5$). This indicates that a faster transition of the near-tip E'_α from E'_1 to E'_3 (see Fig. 2), results in smaller elongation of the fracture footprint (i.e. larger b/a). The effect of the Thomsen parameter δ on the fracture footprint appears relatively small (less than 4% of relative difference) as can be observed from Fig. 8d.

The corresponding self-similar width $\Omega_k = w/W_k$ profiles along the major and the minor axis are shown in Fig. 9. We observe that the fracture width profile appears to be mostly sensitive to β , with little effect of the other dimensionless elastic parameters (C_{13}/C_{11} , and the Thomsen parameters ϵ and δ). Fig. 10 reports the time-evolution of the dimensionless net pressure $p(t)/P_k(t_k)$ for different values of β , C_{13}/C_{11} , Thomsen parameters ϵ and δ (see Figs. 10a,b, c and d respectively).

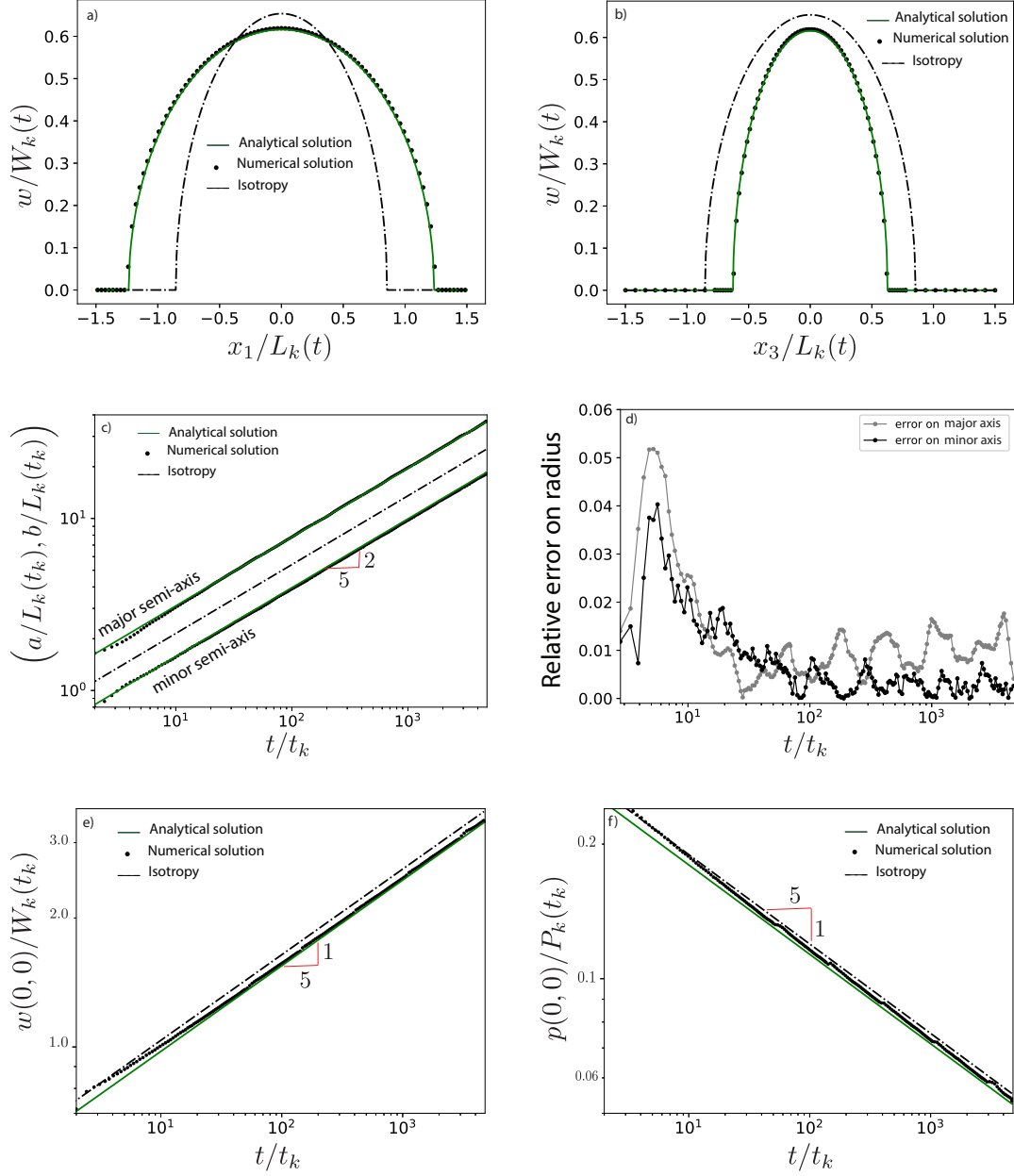


Figure 7: Toughness dominated regime - elliptical toughness anisotropy $\kappa^{-1} = 1.2$, $\beta = 1.2$, $\epsilon = 0.3$, $\delta = 0.2$, and $C_{13}/C_{11} = 0.5$: (a,b) dimensionless self-similar width profile Ω_k along e_1 and e_3 respectively, (c) exhibit the dimensionless length of the major $a(t)/L_k(t_k)$ and minor $b(t)/L_k(t_k)$ semi-axis as well as the relative error with respect to the analytical solution (Appendix A) in (d). (e,f) Time evolution of the dimensionless width $w(0,0)/W_k(t_k)$ and net pressure $p(0,0)/P_k(t_k)$ respectively at the injection.

It evolves with $-1/5$ power law of time, similarly than in the case of isotropic material as anticipated by the scaling analysis. We also directly observe that the dimensionless elastic parameters have little effect on the net pressure, which is close to the radial isotropic toughness dominated solution.

8.3. Isotropic fracture energy

Another possible limiting anisotropic behavior is the case of an isotropic fracture energy $G_c(\alpha) = G_c$. As a result, the fracture toughness $K_{Ic}(\alpha) = \sqrt{G_c E'_\alpha}$ decreases with α in this case, following the variation of the elastic modulus E'_α (see Fig. 2). The toughness ratio, $\kappa = K_{Ic,1}/K_{Ic,3} = \sqrt{\beta}$ is thus greater than 1 such that it partly compensates the effect of elastic anisotropy. Using a similar procedure than before, i.e. matching the width of the toughness dominated near-tip asymptote in the divider and arrester directions ($K_{Ic,1}/E'_1 \sqrt{a} \propto K_{Ic,3}/E'_3 \sqrt{b}$, we now obtain that b/a should be proportional to β^{-1} , compared to β^{-2} for isotropic toughness (Bessmertnykh and Dontsov, 2018; Laubie and Ulm, 2014). A series of simulation for different values of β recover exactly such an estimate as can be seen from Fig 11. Here again, the time-evolution of fracture shape, width and net pressure follows the same power-law of time than the isotropic case as predicted by the scaling analysis. It is worth noting that the effect of the other elastic parameters (besides β) is, similarly than for the isotropic toughness case, rather small and thus not shown here.

8.4. Self-similar fracture shape: planar 3D results versus an approximated elliptical solution

It is interesting to compare our numerical results obtained without any assumptions on the fracture shape to a previous analysis based on the assumption of an elliptical fracture shape (Laubie and Ulm, 2014; Bessmertnykh and Dontsov, 2018). In the toughness dominated regime, where the pressure is uniform, we can use the analytical solution for an elliptical fracture in TI medium (see e.g. Appendix A) and either for the assumption of isotropic K_I or G obtain the aspect ratio b/a by minimizing the variations of K_I , respectively G along the front. Using the approximation E'_{app} (19) in lieu of the exact E'_α (14), Laubie and Ulm (2014); Bessmertnykh and Dontsov (2018) obtained that $b/a \propto \beta^{-1}$ under the assumption of isotropic fracture energy (for weak elastic anisotropy).

Using a similar method as Laubie and Ulm (2014) (using either E'_{app} or the exact E'_α), we can compare the self-similar fracture aspect ratio in the toughness dominated regime using such an approximated "elliptical" fracture approach with our fully coupled numerical solution. We minimize the variations of either K_I or G along the front using a L_1 norm and twenty sample points in a quadrant of the elliptical fracture front.

The evolution of the aspect ratio as function of β are displayed in Fig. 12 for both the fully coupled numerical results (not assuming an elliptical shape) and the minimization assuming an elliptical shape. The complete numerical results (with the exact E'_α) and elliptical approximation follows the trend $b/a \propto \beta^{-2}$ as expected but with different pre-factors. The discrepancy increases significantly for large anisotropy. For $\beta > 1.12$ (i.e. $\beta^{-2} < 0.8$), the aspect ratio given by the elliptical fracture assumption is overestimated by more than 10% compared to the exact numerical results (and more than 30% for strong anisotropy: $\beta^{-2} < 0.45$). For weaker anisotropy ($\beta < 1.12$, i.e. $\beta^{-2} > 0.8$), the two estimations agree well. The numerical results obtained using E'_{app} (blue triangles) as the near-tip modulus for the fully HF coupled problem diverge from the ones obtained using E'_α (green dots) for $\beta^{-2} < 0.6$ ($\beta > 1.3$). They underestimate fracture elongation

Self-similar dimensionless fracture footprint

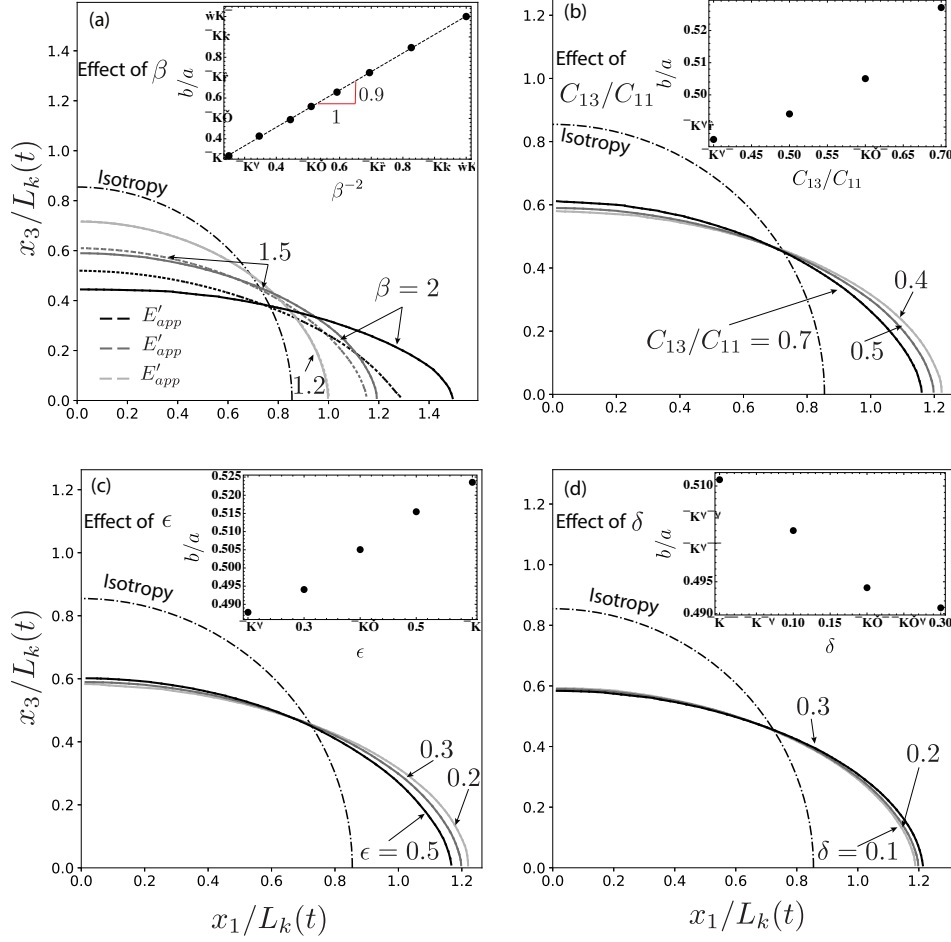


Figure 8: Toughness dominated propagation - isotropic toughness case: self similar footprint γ_k obtained using the exact expression for E'_α (solid line) and the approximation function E'_{app} (dashed line) as the near-tip elastic modulus. Reference parameters: $\beta = 1.5$, $C_{13}/C_{11} = 0.5$, $\epsilon = 0.3$, and $\delta = 0.2$. (a) variations of $\beta = (1.2, 1.5, 2)$, (b) variations of $C_{13}/C_{11} = (0.4, 0.5, 0.7)$, (c) variations of $\epsilon = (0.2, 0.3, 0.5)$, and (d) variations of $\delta = (0.1, 0.2, 0.3)$. The insets display the corresponding evolution of the fracture aspect ratio b/a .

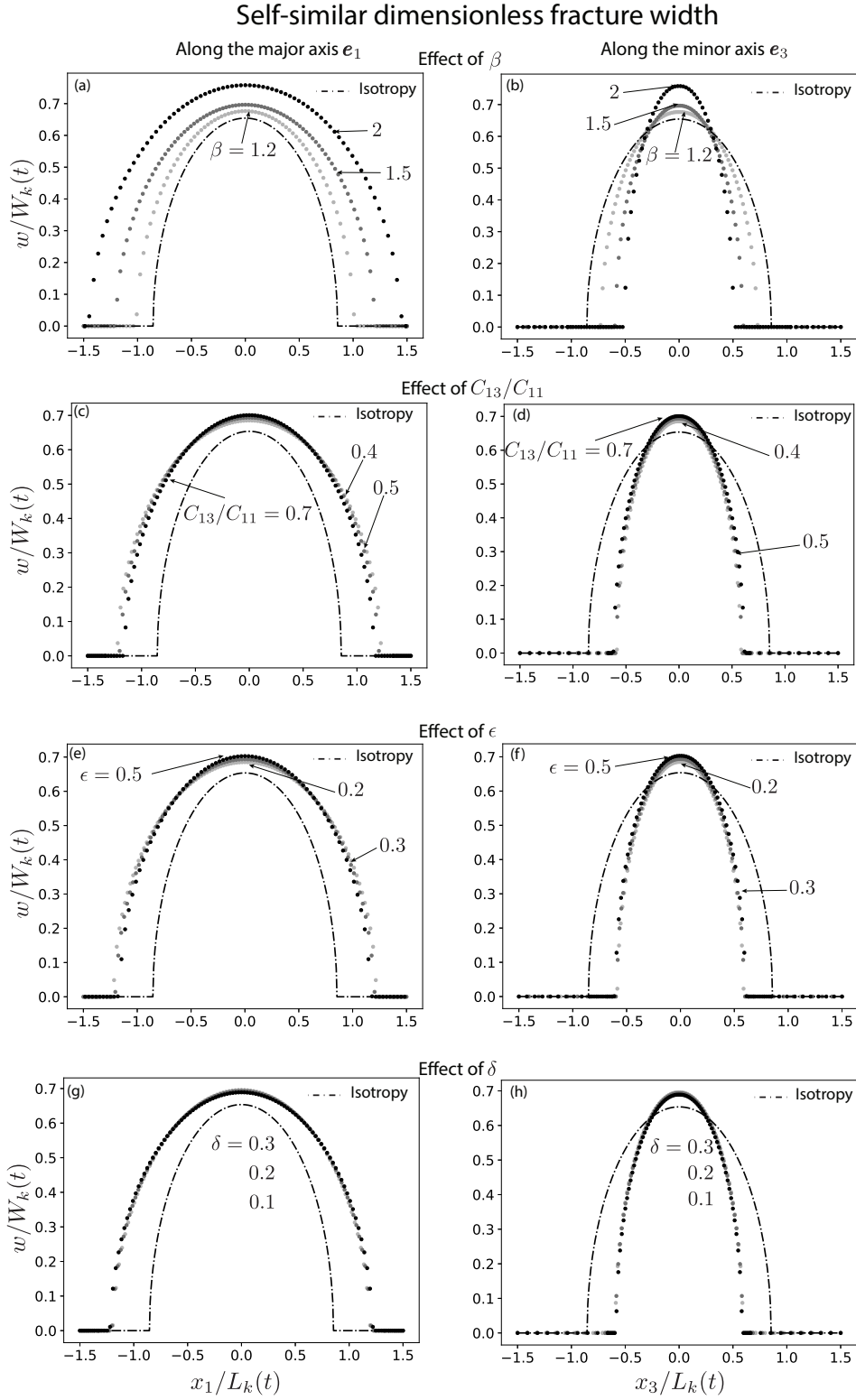


Figure 9: Toughness dominated propagation - isotropic toughness case: self similar width profiles along \mathbf{e}_1 and \mathbf{e}_3 . Reference parameters: $\beta = 1.5$, $C_{13}/C_{11} = 0.5$, $\epsilon = 0.3$, and $\delta = 0.2$. (a, b) variations of $\beta = (1.2, 1.5, 2)$, (c, d) variations of $C_{13}/C_{11} = (0.4, 0.5, 0.7)$, (e, f) variations of $\epsilon = (0.2, 0.3, 0.5)$, and (g, h) variations of $\delta = (0.1, 0.2, 0.3)$.

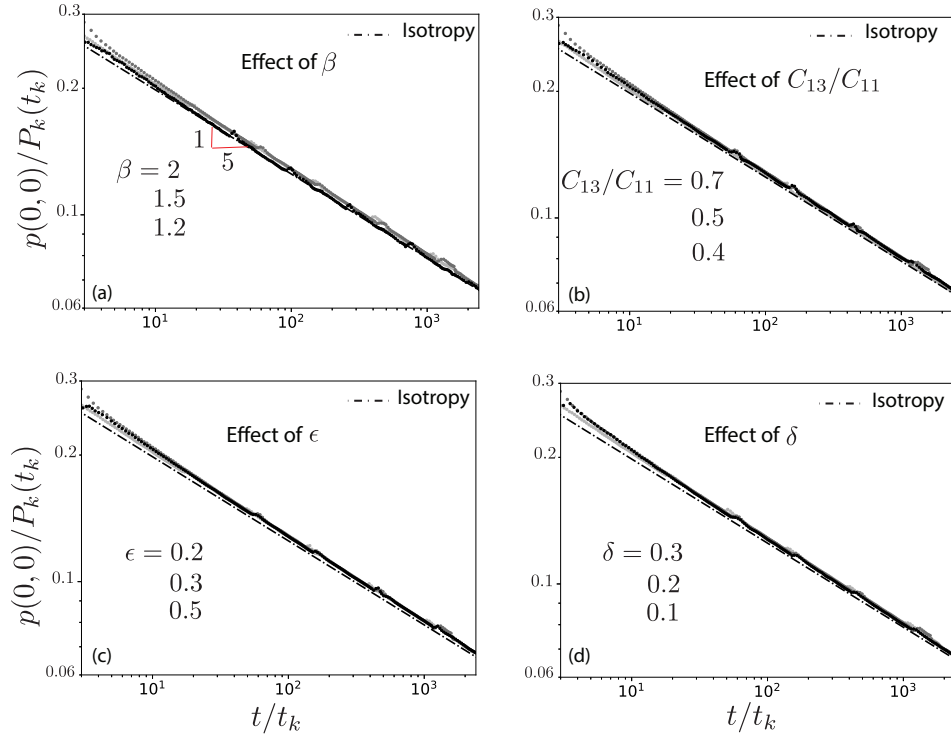


Figure 10: Toughness dominated propagation - isotropic toughness case: dimensionless pressure evolution at the injection point $p(0,0)/P_k(t_k)$ with time t/t_k . Reference parameters: $\beta = 1.5$, $C_{13}/C_{11} = 0.5$, $\epsilon = 0.3$, and $\delta = 0.2$. (a) $\beta = (1.2, 1.5, 2)$, (b) $C_{13}/C_{11} = (0.4, 0.5, 0.7)$, (c) $\epsilon = (0.2, 0.3, 0.5)$, and (d) $\delta = (0.1, 0.2, 0.3)$.

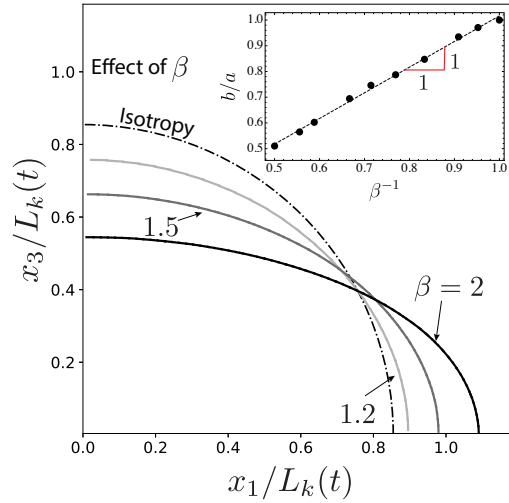


Figure 11: Toughness dominated propagation - isotropic fracture energy case: self similar footprint for different values of $\beta = (1.2, 1.5, 2)$ with $\epsilon = 0.3$, $\delta = 0.2$, and $C_{13}/C_{11} = 0.5$. The inset figure displays the evolution of the fracture aspect ratio b/a as function of β .

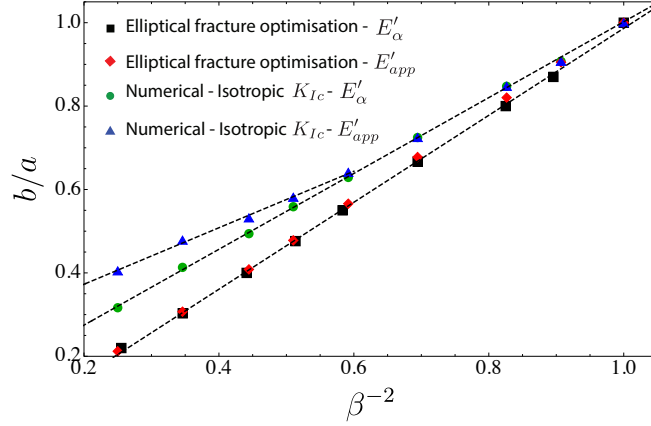


Figure 12: Toughness dominated regime - isotropic toughness: comparison of the fracture aspect ratios b/a obtained from the minimization of the stress intensity factor variation along the front of an elliptical crack using E'_α (black square) or the approximation E'_{app} (red diamond) for the near-tip elastic modulus and results of the numerical solution using E'_α (green dot) or E'_{app} (blue triangles). $\epsilon = 0.3$, $\delta = 0.2$, and $C_{13}/C_{11} = 0.5$ for all cases.

by as much as 45%. The variations of the stress intensity factor along the front of an elliptical fracture obviously never exactly disappear (even after minimization) as only a peculiar form of fracture toughness anisotropy (29) can ensure a exact elliptical shape. Fig. 13 displays the residual variations obtained after minimization. They are smaller for weak elastic anisotropy, and reaches about 7% in relative term for $\beta = 2$.

The results for the hypothesis of an isotropic fracture energy are summarized in Fig. 14. The difference between the elliptical assumption and the complete numerical solution is smaller than for the case of isotropic toughness. All results follow a trend $b/a \propto \beta^{-1}$. The approximated solutions tends to slightly over-estimate the fracture elongation (especially for stronger elastic anisotropy - $\beta^{-1} < 0.7$). The residuals variations of the stress intensity factor along the elliptical crack are smaller than for the hypothesis of isotropic toughness (at most 4% percent for the largest anisotropy).

9. Transition from viscosity to toughness dominated growth

After investigating the hydraulic fracture growth in each of the toughness and viscosity dominated regime, we now focus on the evolution from toughness to viscosity and the time of its occurrence. We compare the numerical results given by the three different toughness variations defined above: elliptical fracture toughness function, isotropic toughness and isotropic fracture energy. The simulations are performed with an initial rectangular domain of 100 cells along \mathbf{e}_1 and 80 cells along \mathbf{e}_3 . The fracture is initiated with the solution of a radial fracture propagating in the viscosity dominated regime. We set the elastic parameters to the following values: $\beta = 1.5$, $C_{13}/C_{11} = 0.5$, $\epsilon = 0.3$, $\delta = 0.2$. We present the numerical results using the viscosity-to-toughness M-K scaling listed in Table 3 where E'_* and K'_* are chosen here to be inline with the arrester direction ($E'_* = E'_1$, $K'_* = K'_1$). We focus here on the evolution of the semi-major and minor axes function of the dimensionless time $t/t_{mk,1}$ (Figs. 15, 16 and 17) as the fracture shape,

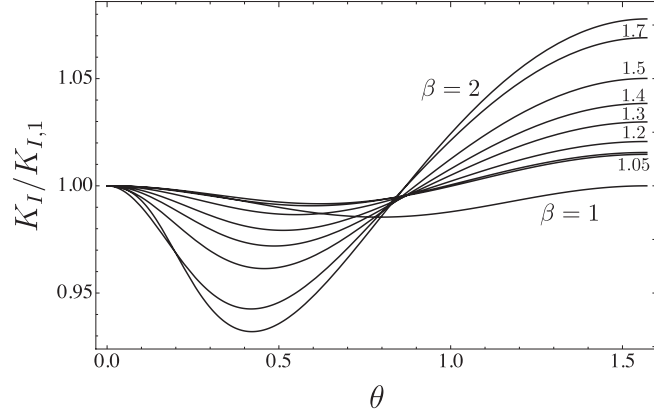


Figure 13: Toughness dominated regime - isotropic toughness: residual of the variation of the scaled stress intensity factor $K_I/K_{I,1}$ after minimization as function of $\theta = \arctan\left(\frac{b}{a}\alpha\right)$ with $\epsilon = 0.3$, $\delta = 0.2$, and $C_{13}/C_{11} = 0.5$ for all cases.

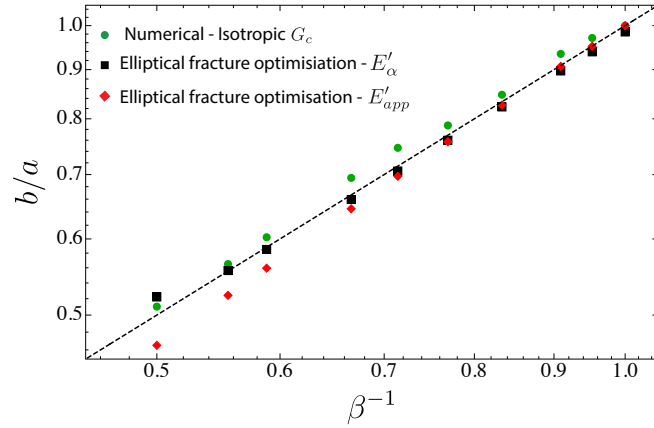


Figure 14: Toughness dominated regime - isotropic fracture energy: comparison of the fracture aspect ratios b/a obtained from the numerical solution (green dot), the fracture energy minimization criterion using E'_α (black square) or the approximation E'_{app} (red diamond) for the near-tip elastic modulus as function of β^{-1} . $\epsilon = 0.3$, $\delta = 0.2$, and $C_{13}/C_{11} = 0.5$ for all cases.

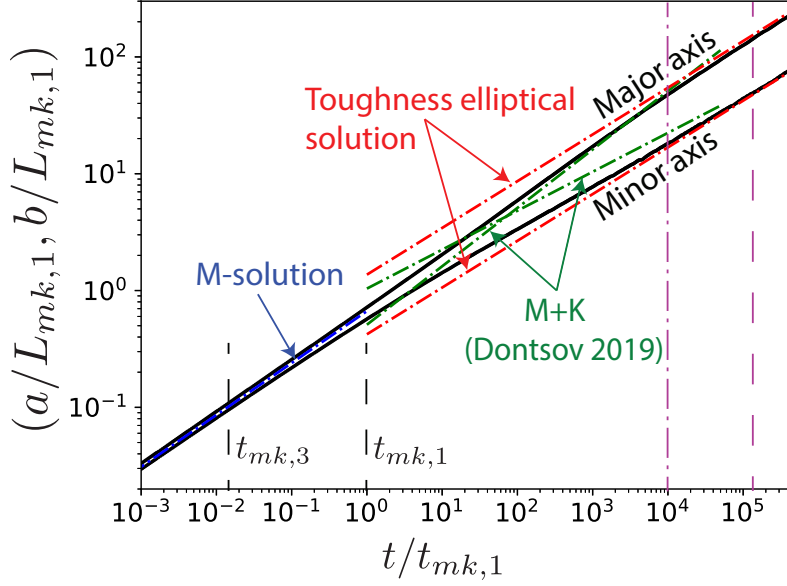


Figure 15: Elliptical toughness - viscosity to toughness transition: time evolution of the dimensionless major $a(t)/L_{mk,1}$ and minor $b(t)/L_{mk,1}$ semi axis for $\kappa^{-1} = 1.2$, $\beta = 1.5$, $\epsilon = 0.3$, $\delta = 0.2$, and $C_{13}/C_{11} = 0.5$.

width and pressure profiles have been already grasped for the limiting regimes previously (sections 7 and 8). We compare our numerical results with the approximated solution M+K (green dot-dashed lines) of Dontsov (2019) obtained by combining the near-tip HF asymptote and the global volume balance assuming an elliptical fracture. This solution (which uses the approximation of E'_{app}) depends only on the elasticity ratio β and the toughness ratio κ . It is applicable for large toughness ratio ($\kappa^{-1} > 10$) in the transitional part when the semi-major axis propagates in the viscosity dominated regime and the minor axis already propagated in the dominated toughness regime (Dontsov, 2019). Nevertheless, we also report this solution in Figs. 15, 16 and 17 for comparison despite the possibly significant error of the approximated solution for small toughness ratio.

We also plot the isotropic radial HF viscosity dominated solution in blue dot-dashed lines using $\langle E' \rangle$ and $\langle K' \rangle$ as the value of the elastic modulus and fracture toughness respectively (M-solution in Figs. 15, 16 and 17). The analytical solution for the elliptical toughness dominated HF (see Appendix A for details) is presented in red dotted-dashed lines. The purple line represent the time at which the numerical results for the major (in dashed) and the minor (in dot-dashed) axis are within 7% of the elliptical HF toughness solution. We use that threshold to define the start of the toughness dominated regime.

9.1. Elliptical toughness

Fig. 15 displays the fracture semi-axis with time for the elliptical toughness anisotropy Eq. (29) for a toughness ratio $\kappa^{-1} = 1.2$. The ratio of the transition time scales of the arrester and divider direction is (see Eq. (27)) $t_{mk,3}/t_{mk,1} = \beta^{-13/2}\kappa^9 = 0.014$. At early time ($t/t_{mk,1} < 1$), the fracture

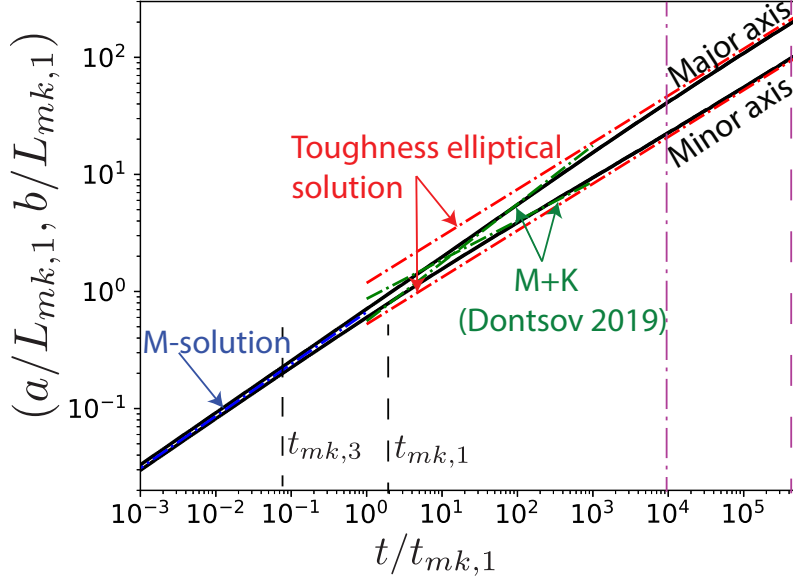


Figure 16: Isotropic toughness ($\kappa = 1$) - viscosity to toughness transition: time evolution of the dimensionless major $a(t)/L_{mk,1}$ and minor $b(t)/L_{mk,1}$ semi axis for $\beta = 1.5$, $\epsilon = 0.3$, $\delta = 0.2$, and $C_{13}/C_{11} = 0.5$.

radius follow closely the isotropic solution of a radial fracture as discussed in section 7. In the intermediate regime $10^2 < t/t_{mk,1} < 10^4$, the approximated M+K solution for the major axis $a(t)$ (Dontsov, 2019) is close to the numerical solution but deviates as soon as the fracture radius reaches the elliptical solution for the toughness regime, while for the minor axis, the two solutions (M+K solution and the numerical solution) are quite apart which can be traced back to the domain of validity of the M+K approximated solution which is accurate only for toughness ratio ($\kappa^{-1} > 10$) much larger than the one used here ($\kappa^{-1} = 1.2$).

The numerical results matches well the exact elliptical HF toughness dominated solution at times larger than $1.3 \times 10^5 t_{mk,1}$. Notably, The numerical fracture shape evolves in the toughness dominated regime with a constant aspect ratio exactly as predicted by equation (31): $b/a = \beta^{-2} \kappa^2 = 3.24$. In terms of dimensionless toughness $\mathcal{K}_1 = (t/t_{mk,1})^{1/9}$ (see Table 3), the major axis reaches the toughness regime within 7% of relative error at $\mathcal{K}_1 \approx 3.7$ ($t \approx 1.3 \times 10^5 t_{mk,1}$), which is consistent with the estimation obtained for the case of isotropy (Savitski and Detournay, 2002). The minor axis reaches the toughness regime when $\mathcal{K}_3 = \mathcal{K}_1 \times (t_{mk,3}/t_{mk,1})^{-1/9} \approx 4.5$ according to Fig. 15 - which corresponds to an earlier time ($t \approx 1.06 \times 10^4 t_{mk,1} = 75 \cdot 10^5 t_{mk,3}$).

9.2. Isotropic toughness

Fig. 16 presents the numerical solution for the semi-major and minor axes assuming an isotropic toughness function. The analytical solution for the toughness dominated elliptical HF is here plotted for the case $\kappa = 1$. The ratio of timescales is now only function of β : $t_{mk,3}/t_{mk,1} = \beta^{-13/2} = (0.07$ for the chosen $\beta = 1.5$). The viscosity dominated regime extends further squeezing the transition to a narrow region. The M+K approximated solution captures the order of magnitude of the evolu-

tion of the major respectively minor axis in a narrow range of times $70 < t/t_{mk,1} < 3 \cdot 10^2$ (major), respectively $10^2 < t/t_{mk,1} < 8 \cdot 10^3$. The slope (power-law) of this approximated solution in both cases clearly do not follow the numerical results - which again is due to the fact that such a M+K solution is only valid for the case of a large toughness anisotropy ($\kappa^{-1} > 10$).

For an isotropic toughness, our numerical solution indicates that the major and minor axis reach the toughness dominated regime for $\mathcal{K}_1 \approx 4.3$ ($t \approx 5 \times 10^5 / t_{mk,1}$) and $\mathcal{K}_3 \approx 3.7$ ($t \approx 10^4 t_{mk,1}$) respectively. The relative difference between the numerical solution and the toughness dominated elliptical HF solution is larger in that case. This is directly related to the fact that the fracture does not have strictly an elliptical shape in the toughness dominated regime as discussed in section 8.4.

9.3. Isotropic fracture energy

The results for the isotropic fracture energy case is given in Fig. 17. The toughness ratio is here a function of the elasticity $\kappa^{-1} = \sqrt{E'_3/E'_1} = \beta^{-1/2}$ ($= 0.8$ for $\beta = 1.5$) which we use for the toughness dominated HF elliptical solution. The ratio of the characteristic timescales now reduces to: $t_{mk,3}/t_{mk,1} = \kappa^9 \beta^{-13/2} = \beta^{-2}$ ($= 0.44$). The effect of anisotropy of toughness and elasticity are not compounded in this case. As a result, the fracture propagates with a smaller aspect ratio ($b/a = \beta^{-1}$) in the toughness dominated regime. The transition to the toughness regime occurs earlier for such an isotropic fracture energy assumption: at $\mathcal{K}_1 \approx 2.9$ ($t \approx 1.4 \times 10^4 t_{mk,1}$) for the major axis, and $\mathcal{K}_3 \approx 1.13$ ($t \approx 1.3 \times 10^4 t_{mk,1}$) for the minor axis. The numerical results at large time follows the elliptical HF toughness dominated solution (with a slight deviation that is barely visible in log-log scale). The fracture shape is not far from being elliptical in that case as discussed in section 8.4. Similarly than for the isotropic toughness, for such a rather low toughness ratio, the approximated M+K solution is out of its domain of validity. It exhibits a different power-law of time for the minor and major axis evolution compared to the fully coupled numerical results.

10. Conclusions

Propagation of a planar HF perpendicular to the isotropy plane is arguably the most common configuration encountered during the stimulation of unconventional hydrocarbon reservoirs. Using a fully coupled HF solver, we have quantified the impact of transverse isotropy on the growth of a hydraulic fracture, notably the elongation of the fracture in the divider direction and its shortening in the arrester direction.

Using a change of reference frame and the solution for a edge dislocation in an orthotropic medium, we have obtained an exact expression of the elastic modulus controlling the near-tip elastic operator (14) as function of the angle between the local fracture propagation direction and the isotropy plane (see Fig. 1). This near-tip elastic modulus enters both in the local near-tip elastic operator and the Irwin matrix relating the energy release rate and the stress intensity factor. This exact expression of the near-tip elastic modulus quantifies the validity of an approximated expression put forward previously (Laubie and Ulm, 2014) which appears to be valid only for weak elastic anisotropy ($\beta \leq 1.2$). As a result, approximated solutions for the growth of a finite HF in a TI material using this approximation in combination with the assumption of an elliptical fracture do compare reasonably well with our fully coupled numerical results only for weak anisotropy

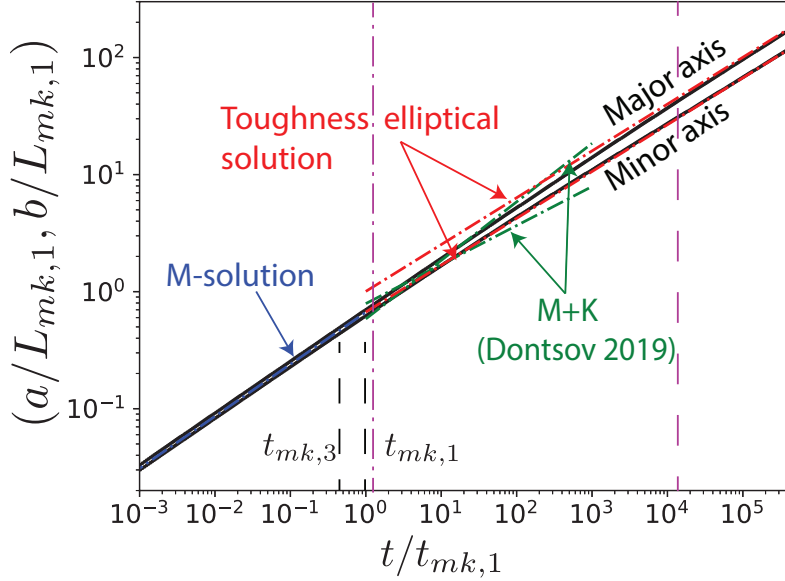


Figure 17: Isotropic fracture energy viscosity to toughness transition: time evolution of the dimensionless major $a(t)/L_{mk,1}$ and minor $b(t)/L_{mk,1}$ semi axis for $\beta = 1.5$, $\epsilon = 0.3$, $\delta = 0.2$, and $C_{13}/C_{11} = 0.5$.

($\beta \leq 1.2$). Assuming the fracture shape to be elliptical overestimates the exact fracture aspect ratio by more than 30% for larger elastic anisotropy ($\beta > 1.5$) and isotropic toughness.

It is important to recall that the fracture has strictly an elliptical shape only for a very peculiar case of toughness anisotropy that can be deduced from the elliptical crack elastic solution (Appendix A). We have derived from the TI elliptical fracture solution, a solution for HF growth in the toughness dominated regime (for such a form of elliptical toughness anisotropy). Our numerical solver perfectly reproduces this toughness dominated solution.

In the viscous dominated regime, toughness does not affect HF growth. Our results show that elastic anisotropy leads to a slight elongation of the fracture in the divider direction in this viscous regime, with aspect ratio scaling as $b/a \approx 0.76\beta^{-1/3}$, confirming the scaling arguments derived in Bessmertnykh and Dontsov (2018). The other dimensionless elastic parameters have a relatively small effect.

In the toughness dominated regime, the fracture is more elongated than in the viscosity dominated regime both for the hypothesis of elliptical toughness, isotropic toughness or isotropic fracture energy. The intensity of the elongation strongly depends on the type of toughness anisotropy. As already mentioned, the fracture is elliptical only when toughness evolves according to eq. (29) where $b/a = (\kappa/\beta)^2$. For an isotropic toughness ($\kappa = 1$), the aspect ratio evolves as $b/a \approx 0.9\beta^{-2}$, consistent with the ratio of the LEFM asymptote between the orthogonal directions (\mathbf{e}_1 and \mathbf{e}_3). The other elastic parameters have a second order effect (at most about 10% of variation). The elongation is less pronounced for the case of an isotropic critical fracture energy, where $b/a \approx \beta^{-1}$. Here again the other elastic parameters do not impact fracture growth significantly.

We have explored numerically (for a given set of elastic coefficients), the transition between the

viscosity and toughness dominated regimes. Our results confirm the expression of the transition time-scales $t_{mk,1}$ and $t_{mk,3}$ obtained from scaling considerations. The ratio of these time-scales $t_{mk,3}/t_{mk,1} = \beta^{-13/2}\kappa^9$ govern how early fracture elongation start to increase from its initial value in the viscosity dominated regime. The exact time at which the toughness regime is reached depends on the type of toughness evolution. However, to first order it is consistent with the limit obtained for isotropy (Savitski and Detournay, 2002): i.e $\mathcal{K} > 3.5$ for toughness dominated growth.

The extension of the implicit level set algorithm to account for transverse isotropy has proven robust for all realistic values of material properties investigated here. It provides a robust solution for planar 3D HF growth in TI. Of course, extreme anisotropy $\beta > 2$ causes numerical difficulties as the fracture curvature becomes extreme in the divider direction (\mathbf{e}_1) thus requiring finer discretization.

For practical applications, the variation of fracture toughness as function of the local propagation direction (angle α) is clearly of first importance, as already pointed out for the elastic isotropy / toughness anisotropic case (Zia et al., 2018). Our results reinforce the need for better experimental characterization of the mode I fracture toughness of TI material in different directions. Unfortunately, such laboratory measurements are rare and often focus mostly on the plane-strain case of a planar crack propagating at angle with the isotropy plane, and not for different value of α as per the configuration of Fig. 1. Our results indicate a positive effect of anisotropy on vertical containment of hydraulic fractures propagating in finely layered sedimentary formation: a possible explanation for the small vertical extent of HFs in finely layered sedimentary rock even in the absence of in-situ stress contrast. Ultimately, laboratory experiments of HF growth in TI materials with proper measurements of the evolution of the fracture shape are required to further test the theoretical results presented here.

Acknowledgments. This work was funded by the Swiss National Science Foundation under grant #160577.

References

- Barnett, D., Asaro, R., 1972. The fracture mechanics of slit-like cracks in anisotropic elastic media. *Journal of the Mechanics and Physics of Solids* 20, 353–366.
- Barnett, D., Swasger, L., 1971. The elastic energy of a straight dislocation in an infinite anisotropic elastic medium. *Physica Status Solidi (b)* 48, 419–428.
- Batchelor, G., 1967. *An Introduction to Fluid Dynamics*. Cambridge University Press, Cambridge, UK.
- Bessmertnykh, A., Dontsov, E., 2018. Aspect ratio of hydraulic fracture in homogeneous transversely isotropic material, in: 52nd US Rock Mechanics/Geomechanics Symposium, American Rock Mechanics Association.
- Bobko, C., Ulm, F., 2008. The nano-mechanical morphology of shale. *Mechanics of Materials* 40, 318–337.
- Bonnet, M., 1999. *Boundary integral equation methods for solids and fluids*. volume 34. Wiley-Blackwell ed., Springer.
- Bunger, A.P., Lecampion, B., 2017. Four critical issues for successful hydraulic fracturing applications, in: Feng, X.T. (Ed.), *Rock Mechanics and Engineering*. CRC Press/Balkema. volume 5 (Surface and Underground Projects). chapter 16.
- Chertov, M., 2012. Closed-form solution for vertical fracture width in anisotropic elastic formations. *International Journal of Rock Mechanics and Mining Sciences* 53, 70–75.
- Cho, J., Kim, H., Jeon, S., Min, K., 2012. Deformation and strength anisotropy of asan gneiss, boryeong shale, and yeoncheon schist. *International Journal of Rock Mechanics and Mining Sciences* 50, 158–169.
- Desroches, J., Detournay, E., Lenoach, B., Papanastasiou, P., Pearson, J.R.A., Thiercelin, M., Cheng, A., 1994. The crack tip region in hydraulic fracturing. *Proceedings of the Royal Society of London. Series A: Mathematical and Physical Sciences* 447, 39–48. URL: <http://rspa.royalsocietypublishing.org/content/447/1929/39.short>.
- Detournay, E., 2004. Propagation regimes of fluid-driven fractures in impermeable rocks. *International Journal of Geomechanics* 4, 35–45. doi:10.1061/(ASCE)1532-3641(2004)4:1(35).
- Detournay, E., 2016. Mechanics of hydraulic fractures. *Annual Review of Fluid Mechanics* 48, 311–339.
- Detournay, E., Peirce, A.P., 2014. On the moving boundary conditions for a hydraulic fracture. *International Journal of Engineering Science* 84, 147–155.
- Dontsov, E., 2019. Scaling laws for hydraulic fractures driven by a power-law fluid in homogeneous anisotropic rocks. *International Journal for Numerical and Analytical Methods in Geomechanics* 43, 519–529.
- Dontsov, E., Peirce, A., 2017. A multiscale implicit level set algorithm (ILSA) to model hydraulic fracture propagation incorporating combined viscous, toughness, and leak-off asymptotics. *Computer Methods in Applied Mechanics and Engineering* 313, 53 – 84.
- Eshelby, J., Read, W., Shockley, W., 1953. Anisotropic elasticity with applications to dislocation theory. *Acta metallurgica* 1, 251–259.
- Fabrikant, V., 2015. General flat crack located in the plane perpendicular to the planes of isotropy in transversely isotropic body. *Acta Mechanica* 226, 3289–3306.
- Gao, H., Rice, J.R., 1987. Somewhat circular tensile cracks. *International Journal of Fracture* 33, 155–174.
- Garagash, D., Detournay, E., 2000. The tip region of a fluid-driven fracture in an elastic medium. *ASME Journal of Applied Mechanics* 67, 183–192.
- Garagash, D., Detournay, E., Adachi, J., 2011. Multiscale tip asymptotics in hydraulic fracture with leak-off. *Journal of Fluid Mechanics* 669, 260–297.
- Hakala, M., Kuula, H., Hudson, J., 2007. Estimating the transversely isotropic elastic intact rock properties for in situ stress measurement data reduction: a case study of the olkiluoto mica gneiss, finland. *International Journal of Rock Mechanics and Mining Sciences* 44, 14–46.
- Hills, D.A., Kelly, P.A., Dai, D.N., Korsunsky, A.M., 1996. Solution of crack problems: the distributed dislocation technique. volume 44 of *Solid Mechanics and its Applications*. Kluwer Academic Publ., Dordrecht.
- Hirth, J.P., Lothe, J., 1982. *Theory of dislocations*. John Wiley and Sons, Inc.
- Hoenig, A., 1978. The behavior of a flat elliptical crack in an anisotropic elastic body. *International Journal of Solids and Structures* 14, 925–934.
- Hubbert, M.K., Willis, D., 1957. Mechanics of hydraulic fracturing. *Trans. Am. Inst. Min. Eng.* 210, 153–158.

- Kanaun, S., Levin, V., 2009. Elliptical cracks arbitrarily oriented in 3d-anisotropic elastic media. *International Journal of Engineering Science* 47, 777–792.
- Keer, L., Lin, W., 1990. Analysis of cracks in transversely isotropic media, in: *Micromechanics and Inhomogeneity*. Springer, pp. 187–195.
- Laubie, H., 2013. Linear elastic fracture mechanics in anisotropic solids: Application to fluid-driven crack propagation. Master's thesis. Massachusetts Institute of Technology.
- Laubie, H., Ulm, F., 2014. Irwin's conjecture: Crack shape adaptability in transversely isotropic solids. *Journal of the Mechanics and Physics of Solids* 68, 1–13.
- Lecampion, B., Bunger, A.P., Zhang, X., 2018. Numerical methods for hydraulic fracture propagation: A review of recent trends. *Journal of Natural Gas Science and Engineering* 49, 66–83. doi:10.1016/j.jngse.2017.10.012.
- Lecampion, B., Peirce, A.P., Detournay, E., Zhang, X., Chen, Z., Bunger, A.P., Detournay, C., Napier, J., Abbas, S., Garagash, D., Cundall, P., 2013. The impact of the near-tip logic on the accuracy and convergence rate of hydraulic fracture simulators compared to reference solutions, in: *The International Conference for Effective and Sustainable Hydraulic Fracturing*, May 20–22, Brisbane, Australia.
- Lin, W., Keer, L., 1989. Three-dimensional analysis of cracks in layered transversely isotropic media. *Proceedings of the Royal Society of London A: Mathematical, Physical and Engineering Sciences* 424, 307–322.
- Malén, K., Lothe, J., 1970. Explicit expressions for dislocation derivatives. *Physica status solidi (b)* 39, 287–296.
- Mogilevskaya, S.G., 2014. Lost in translation: Crack problems in different languages. *International Journal of Solids and Structures* 51, 4492–4503.
- Pan, E., Yuan, J., Chen, W., Griffith, W., 2014. Elastic deformation due to polygonal dislocations in a transversely isotropic half-space. *Bulletin of the Seismological Society of America* 104, 2698–2716.
- Pan, Y., Chou, T., 1976. Point force solution for an infinite transversely isotropic solid. *Journal of Applied Mechanics* 43, 608–612.
- Peirce, A., 2015. Modeling multi-scale processes in hydraulic fracture propagation using the implicit level set algorithm. *Computer Methods in Applied Mechanics and Engineering* 283, 881 – 908.
- Peirce, A., Detournay, E., 2008. An implicit level set method for modeling hydraulically driven fractures. *Computer Methods in Applied Mechanics and Engineering* 197, 2858–2885.
- Peirce, A.P., 2016. Implicit level set algorithms for modelling hydraulic fracture propagation. *Philosophical Transactions of the Royal Society of London A: Mathematical, Physical and Engineering Sciences* 374, 20150423.
- Rice, J., 1985. First-order variation in elastic fields due to variation in location of a planar crack front. *Journal of Applied Mechanics* 52, 571–579.
- Savitski, A., Detournay, E., 2002. Propagation of a penny-shaped fluid-driven fracture in an impermeable rock: asymptotic solutions. *International Journal of Solids and Structures* 39, 6311–6337.
- Sone, H., Zoback, M., 2013. Mechanical properties of shale-gas reservoir rocks—part 1: Static and dynamic elastic properties and anisotropy. *Geophysics* 78, D381–D392.
- Stroh, A., 1958. Dislocations and cracks in anisotropic elasticity. *Philosophical magazine* 3, 625–646.
- Thomsen, L., 1986. Weak elastic anisotropy. *Geophysics* 51, 1954–1966.
- Thöny, R., 2014. Geomechanical analysis of excavation-induced rock mass behavior of faulted Opalinus Clay at the Mont Terri Underground Rock Laboratory (Switzerland). Ph.D. thesis. Diss., Eidgenössische Technische Hochschule ETH Zürich, Nr. 21415.
- Wang, Z., 2002. Seismic anisotropy in sedimentary rocks, part 2: Laboratory data. *Geophysics* 67, 1423–1440.
- Zia, H., Lecampion, B., 2019. PyFrac: a planar 3D hydraulic fracturing simulator. submitted to *Comp. Phys. Comm.*, preprint arXiv:1908.10788v2 .
- Zia, H., Lecampion, B., Zhang, W., 2018. Impact of the anisotropy of fracture toughness on the propagation of planar 3D hydraulic fracture. *International Journal of Fracture* 211, 103–123.

Appendix A. The elliptical hydraulic fracture in a TI material

Appendix A.1. Elliptical fracture under uniform pressure

Eshelby et al. (1953) has shown that for an elliptical fracture in anisotropic media with semi-

major axis a and semi-minor axis b under an uniform pressure p , the fracture opening takes the form:

$$w = B_o p \sqrt{ab} \sqrt{1 - \frac{x_1^2}{a^2} - \frac{x_3^2}{b^2}} \quad (\text{A.1})$$

where B_o is a constant function of the elastic parameter yet to be determined. A number of solutions have been derived in the literature (Fabrikant, 2015; Hoenig, 1978; Kanaun and Levin, 2009, among others), but we have noticed some discrepancies and therefore re-derive it here following Laubie and Ulm (2014) but using the exact near-tip plane-strain modulus E'_α (see section 3). Additionally, an approximation solution using the E'_{app} can be found in Dontsov (2019).

First we define $A^f(x_1^f, x_3^f)$ as the projection on the fracture front of a point $A(x_1, x_3)$ inside the fracture. We denote $|x'_1|$ as the distance between these two points and α the angle between the major axis \mathbf{e}_1 and the local axis \mathbf{e}'_1 as described in Fig. 1. Using the geometrical properties of the ellipse

$$\tan \alpha = \frac{a^2}{b^2} \frac{x_3}{x_1} \quad (\text{A.2})$$

we obtain the first order expansion:

$$1 - \frac{x_1^2}{a^2} - \frac{x_3^2}{b^2} = 2|x'_1| \left(\frac{x_1^f \cos \alpha}{a^2} + \frac{x_3^f \sin \alpha}{b^2} \right) + O(x_1'^2) \quad (\text{A.3})$$

Introducing the polar angle characterizing the ellipse:

$$x_1^f = a \cos \theta \quad x_3^f = b \sin \theta \quad (\text{A.4})$$

such that from Eq. (A.2), we have the correspondance:

$$\tan \alpha = \frac{a}{b} \tan \theta \quad (\text{A.5})$$

Eq. (A.3) can thus be re-written as:

$$1 - \frac{x_1^2}{a^2} - \frac{x_3^2}{b^2} = 2|x'_1| \left(\frac{\cos^2 \theta}{a^2} + \frac{\sin^2 \theta}{b^2} \right)^{1/2} + O(x_1'^2) \quad (\text{A.6})$$

We thus obtain the first order term asymptote of the near-tip fracture opening (A.1) as:

$$w = B_o p \sqrt{b} \sqrt{2|x'_1|} \left(\sin^2 \theta + \left(\frac{b}{a} \right)^2 \cos^2 \theta \right)^{1/4}, \quad |x'_1| \ll a, |x'_1| \ll b \quad (\text{A.7})$$

The stress intensity factor along the elliptical front can thus be obtained by equalizing the previous equation to the classical LEFM near-tip asymptote (20):

$$K_I = \frac{B_o}{4} \sqrt{\pi a} E'_\alpha p \left(\sin^2 \theta + \left(\frac{b}{a} \right)^2 \cos^2 \theta \right)^{1/4}. \quad (\text{A.8})$$

758 The global fracture energy \mathcal{G} , on the other hand, is given by the derivative of the work W with
 759 respect to the crack extension area under constant load:

$$\mathcal{G} = \frac{1}{2\pi b} \frac{\partial W}{\partial a} = \frac{1}{2\pi b} \frac{\partial}{\partial a} \left(\frac{1}{2} p V_{frac} \right) = \frac{1}{2} p^2 b a^{1/2} B_o \quad (\text{A.9})$$

760 where $V_{frac} = \frac{2}{3} \pi a b B_o$ is the fracture volume. The global fracture energy \mathcal{G} can also be estimated
 761 from the integral of the local energy release rate along the crack front which for a mode I fracture
 762 in our configuration reduces to:

$$\mathcal{G} = \frac{1}{2\pi} \int_0^{2\pi} \frac{K_I^2(\alpha(\theta))}{E'_\alpha(\alpha(\theta))} d\theta. \quad (\text{A.10})$$

763 Following Hoenig (1978), we recover the opening pre-factor B_o from the two expressions of the
 764 global fracture energy (A.9) and (A.10):

$$B_o = 16 \left(\frac{b}{a} \right)^{1/2} \frac{1}{\int_0^{2\pi} E'_\alpha(\alpha(\theta)) \times \left((b/a)^2 \cos^2 \theta + \sin^2 \theta \right)^{1/2} d\theta}. \quad (\text{A.11})$$

765 which needs to be evaluated numerically using the expression of E'_α (14). For the isotropic elastic
 766 case, B_o is obtained analytically function of the complete elliptical integral of the second kind
 767 $\mathbb{E}(\sqrt{1 - (b/a)^2})$ (Gao and Rice, 1987; Hills et al., 1996, among others).

$$B_{o,iso} = \frac{4}{E'_{iso} \mathbb{E}(\sqrt{1 - (b/a)^2})} \left(\frac{b}{a} \right)^{1/2} \quad (\text{A.12})$$

768 Appendix A.2. Elliptical hydraulic fracture - toughness dominated solution

769 From the previous elastic solution, it is rather simple to obtain a growth solution for a hydraulic
 770 fracture in the toughness dominated regime. We write $K_{Ic,3}$ as the material toughness in the divider
 771 direction \mathbf{e}_3 and E'_3 the corresponding near-tip elastic modulus. First, to ensure a self similar
 772 growth of an elliptical fracture, the toughness must be equal to the stress intensity factor (A.8) at
 773 all points along the fracture front. The toughness variation must therefore has *exactly* the following
 774 form:

$$K_{Ic}(\alpha(\theta)) = K_{Ic,3} \frac{E'_\alpha}{E'_3} \left(\sin^2 \theta + \left(\frac{b}{a} \right)^2 \cos^2 \theta \right)^{1/4} \quad (\text{A.13})$$

775 From the previous equation, we directly obtain the relation between the ellipse aspect ratio (at
 776 $\theta = 0, \pi/2$) and the ratios $\beta = E'_1/E'_3$ and $\kappa = K_{Ic,1}/K_{Ic,3}$:

$$\frac{b}{a} = \left(\frac{K_{Ic,1}}{K_{Ic,3}} \frac{E'_3}{E'_1} \right)^2 = \left(\frac{\kappa}{\beta} \right)^2. \quad (\text{A.14})$$

777 Under quasi-static propagation, $K_I = K_{Ic}$ at all times such that Eqs. (A.8) and (A.13) provide the
 778 following expression for the net pressure:

$$p(t) = \frac{4K_{Ic,3} \sqrt{a/b}}{B_o E'_3 \sqrt{\pi b(t)}}, \quad (\text{A.15})$$

36

779 The evolution of the semi- minor and major axis can then be obtained by enforcing the fact that for
 780 an impermeable medium the volume of the fracture must be equal to injected volume: $V_{frac} = Q_o t$.
 781 We then obtain:

$$b(t) = \left(\frac{3tQ_o E'_3(b/a)}{8K_{Ic,3} \sqrt{\pi}} \right)^{2/5}, \quad a(t) = \left(\frac{K_{Ic,3} E'_1}{K_{Ic,1} E'_3} \right)^2 b(t) \quad (\text{A.16})$$

782 which complete the solution.